Approved for Public Release, Distribution Unlimited

Ultra-wideband Propagation Measurements and Channel Modeling

DARPA NETEX Program

Report on

Through-the-Wall Propagation and Material Characterization

Ahmad Safaai-Jazi, Sedki M. Riad, Ali Muqaibel, and Ahmet Bayram

Time Domain and RF Measurement Laboratory
Bradley Department of Electrical Engineering
Virginia Polytechnic Institute and State University
Blacksburg, Virginia 24061-0111

November 18, 2002

Summary

Ultra wideband (UWB) wireless communication has been the subject of extensive research in recent years due to its potential applications and unique capabilities. However, many important aspects of UWB-based communication systems have not yet been thoroughly investigated. In particular, indoor channel modeling, interference effects, and the role of antennas require careful examinations before an actual implementation of UWB systems can be undertaken. The propagation of UWB signals in indoor and indoor-outdoor environments is the single most important issue with significant impacts on the future direction, scope, and generally the extent of the success of UWB technology. At a fundamental level, the propagation of UWB signals, as any electromagnetic wave, is governed, among other things, by the properties of materials in the propagation medium. Thus, the information on electromagnetic properties of building materials in the UWB frequency range would provide valuable insights in appreciating the capabilities and limitations of UWB technology for indoor and indoor-outdoor applications. Although electromagnetic properties of certain building materials over relatively narrow frequency ranges are available, ultra-wideband characterization of most typical building materials for UWB communication purposes has not been reported.

One of the objectives of this research is to examine propagation through walls made of typical building materials and thereby acquire ultra wideband characterization of these materials. The loss and the dielectric constant of each material are measured over a frequency range of 1 to 15 GHz. Ten commonly used building materials are chosen for this investigation. These include, dry wall, wallboard, structure wood, glass sheet, bricks, concrete blocks, reinforced concrete (as pillar), cloth office partition, wooden door, and styrofoam slab. The characterization method is based on measuring an *insertion transfer function*, defined as the ratio of two signals measured in the presence and in the absence of the material under test. The insertion transfer function is related to the dielectric constant of the material through a complex transcendental equation which can be solved using numerical two-dimensional root search techniques. The insertion transfer function can be obtained either through frequency-domain measurements using a vector network analyzer, or by performing time-domain measurements using a pulse generator and a sampling oscilloscope and then Fourier transforming the measured signals into the frequency domain. Here, both frequency-domain and time-domain measurement techniques are used in order to validate the results and ensure the accuracy of measurements. The results for the dielectric constant and loss of the measured materials are presented graphically and numerically as lookup tables. The data can be used for studying channel modeling problems.

In addition to successfully carrying out ultra wideband characterization of building materials, this investigation resulted in another interesting contribution. As mentioned above, the dielectric constant is determined by solving a complex transcendental equation, a process which

is often time consuming due to slow convergence and the existence of spurious solutions. We found a new formulation for evaluating the complex dielectric constant of low-loss materials which involves solving real equation and thus requiring only one-dimensional root search techniques. The results derived from the exact complex equation and the new formulation are in excellent agreement. The new formulation reduces the computation time significantly and is highly accurate for the characterization of low-loss materials.

Table of Contents

Table of Figures

1. Introduction

The introduction of UWB communication promises an excellent indoor alternative due to the expected through-the-wall propagation capabilities. The main reason is low signal attenuation at low frequencies. However, to avoid interference with existing systems the bandwidth of operation should be shifted to frequencies above 3 GHz. In this report, quantitative results versus frequency are given for the delay and loss associated with the propagation through typical walls encountered in indoor environments. Results of this research provide valuable insights into the transient behavior of a pulse as it propagates through typical construction materials and structures. Some research work has been performed at the statistical level with the aim of characterizing the UWB communication channel. The results of these studies cannot be validated or explained due to the lack of understanding of basic characteristics of pulse propagation in typical UWB communication environments. A study of propagation through different materials and scatterers would facilitate the development of a basic theory for pulse shaping, receiver design, and channel modeling. Though there has been some research on pulse propagation in the radar field and related electromagnetic aspects, this study has a unique communication flavor.

Generally speaking, material characterization is performed using different techniques, including capacitor, resonator, and coaxial cavities methods, and radiated measurements as well [Bak98]. This work concentrates on ultra wideband signal propagation through different materials and structures and measures their characteristics as they are encountered in the actual UWB communication applications. Radiated measurements allow for non-destructive and broad-band applications [Zha01]. The importance of the measurements in hand stems from the fact that the data available above 1 *GHz* are not adequate for UWB material characterization. Some data at specific frequencies are available through studies of wireless communication inside buildings. Many researchers have examined propagation through walls and floors, but these data are often limited to specific frequency ranges and are also limited to only few materials, thus not adequate for the proposed ultra wideband applications. Moreover, with the inconsistency in published results, understanding and characterization of UWB propagation through walls and in building environments become more compelling.

In this report, the effects of structures as well as materials on UWB propagation are investigated. Some typical obstacles and materials encountered in the indoor wireless propagation channel are studied. These include wooden doors, concrete blocks, reinforced concrete pillars, glass, brick walls, dry walls, and wallboards. In addition to the time-domain

transient response, for some materials the following information is also presented: insertion transfer function (impulse response), relative permittivity, loss tangent, attenuation coefficient, and time delay. Measured data are provided for a frequency range of 1 to 15 GHz. Both frequency-domain and time-domain measurement techniques are used to validate the results and also capitalize on the advantages of each technique.

In section 2 the electromagnetic theory of wave propagation through a material slab is reviewed. Then, the measurement procedure and the techniques used to relate the acquired data to the electrical parameters of materials are discussed in sections 3 and 4. Comparison of results obtained from various techniques for a sample material is presented in section 5. Section 6 is devoted to a comprehensive discussion of the signal processing required to extract the parameters. Detailed descriptions and dimensions for sample materials to be tested are given in Section 7. Main results and observations are presented in Section 8. Additional measurement issues such as distance between the antennas and the sample, repeatability, and variability are also addressed in this section. Finally, section 10 includes some remarks on pulse shaping, UWB receiver design, and modeling hints are given. Two appendices provide details of some mathematical analyses and additional results. Appendix A is dedicated to theoretical analyses and derivations, while Appendix B is devoted to additional results and miscellaneous issues.

2 Propagation of Electromagnetic Waves in Dielectric Materials

In this section, propagation of electromagnetic waves through a lossy dielectric material is reviewed and important parameters are defined. Assuming steady-state time-harmonic electromagnetic fields, a TEM (***t***ransverse ***e***lectro***m***agnetic) plane wave propagating in the $+z$ direction can be represented using the phasor expression $E(z,\omega) = E_0 e^{-\gamma z}$, where $\omega = 2\pi f$ is the radian frequency (f is the frequency in Hz) and γ is the complex propagation constant given as

$$\gamma(\omega) \equiv \alpha(\omega) + j\beta(\omega) = j\omega\sqrt{\mu\varepsilon}\,. \tag{1}$$

where $\alpha(Np/m)$ is the attenuation constant, $\beta(rad/m)$ denotes the phase constant, and ε and μ are, respectively, permittivity and permeability of the material. For non-magnetic materials $\mu = \mu_r \mu_0 \cong \mu_0$ can be safely assumed.

The dielectric polarization loss may be accounted for by a complex permittivity $\varepsilon(\omega) \equiv \varepsilon'(\omega) - j\varepsilon''(\omega)$, where $\varepsilon' = \varepsilon_r \varepsilon_0$ is the real permittivity with ε_r being the relative permittivity constant (≥ 1). The imaginary part of the complex permittivity, ε'', represents the dielectric loss. The dielectric loss is also represented by a parameter referred to as 'loss tangent'

and is defined as $p(\omega) = \tan\delta \equiv \varepsilon''(\omega)/\varepsilon'(\omega)$. It should be noted form (1) that the attenuation constant and the phase constant are both functions of the complex permittivity.

The conductivity loss can be modeled by an additional imaginary term in the complex permittivity, $\varepsilon(\omega) = \varepsilon' - j\left(\varepsilon'' + \sigma/\omega\right)$, where $\sigma(\omega)$ is the macroscopic conductivity of the material of interest. The conductivity loss cannot be easily separated from the dielectric loss but the two losses may be combined and represented by an effective loss tangent [Poz98],

$$p_e(\omega) = \frac{\varepsilon'' + \sigma/\omega}{\varepsilon'} = \frac{\varepsilon''}{\varepsilon'} + \frac{\sigma}{\omega\varepsilon'}. \tag{2}$$

A complex effective relative permittivity can now be defined as

$$\varepsilon_{re}(\omega) = \varepsilon_r(\omega)\left[1 - jp_e(\omega)\right]. \tag{3}$$

To characterize any subsurface material, two parameters should be measured:

- the dielectric constant, $\varepsilon_r(\omega)$
- the effective loss tangent $p_e(\omega)$, or a directly related parameter.

The complex propagation constant is then given by

$$\gamma(\omega) = \frac{j\omega}{c}\sqrt{\varepsilon_{re}} = \frac{j\omega}{c}\sqrt{\varepsilon_r(1 - jp_e)}, \tag{4}$$

where $c = 1/\sqrt{\mu_0\varepsilon_0} \cong 3\times10^8\, m/s$ is the speed of light in vacuum. For a TEM plane-wave propagating inside the material, the attenuation coefficient and the phase constant can be separated in the exponent

$$E(z,\omega) = E_0 e^{-\gamma(\omega)z} = E_0 e^{-j\beta(\omega)z} e^{-\alpha(\omega)z}. \tag{5}$$

The attenuation constant is given by

$$\alpha(\omega) = \frac{\omega}{c}\left\{\frac{\varepsilon_r}{2}\left[\sqrt{1 + p_e^2} - 1\right]\right\}^{1/2} \; Np/m, \tag{6}$$

while the phase constant becomes

$$\beta(\omega) = \frac{\omega}{c}\left\{\frac{\varepsilon_r}{2}\left[\sqrt{1+p_e^2}+1\right]\right\}^{1/2} \; rad/m. \tag{7}$$

A more widely used unit for the attenuation constant α is *dB/m.* The conversion to *dB/m* is simply made using the relationship

$$\alpha(dB/m) = 20\log(e)\alpha(Np/m) = 8.686\alpha(Np/m)\,. \tag{8}$$

At low frequencies, the loss due to ionic conductivity is dominant. But for the frequency range of interest here, which is above 1GHz, water dipolar relaxation becomes the significant loss mechanism. It is pointed out that if the water content of the material is high then the dielectric property is dominated more by the moisture content rather than by the material itself. In general, practical subsurfaces can be considered as mixture of a variety of materials contributing to the effective permittivity [Aur96]. In the next section, the procedures and corresponding setups for measuring the complex dielectric constant are presented.

3 Measurement Procedures

Radiated transmission measurement is used because it allows one to find both the attenuation constant and dispersion of the material under test. Moreover, it provides direct insight into how a critical role through-the-wall propagation plays in UWB communications. The measurement can be performed in time-domain or in frequency-domain. In the time-domain approach, an electromagnetic pulse, $E_i(t, z)$, is applied to a homogenous, isotropic material layer of thickness d. The incident pulse gives rise to a reflected pulse, $E_r(t,z)$, and a transmitted pulse, $E_t(t,z)$. The diagram of the experiment is illustrated in Figure 1. The transmission scattering parameter is then related to the incident and transmitted signals by,

$$S_{21}(j\omega) = \frac{FFT\{v_t(t)\}}{FFT\{v_i(t)\}}, \tag{9}$$

where v_t is the voltage at the output terminals of the receive antenna and is proportional to E_t , while v_i is the voltage at the input terminals of the transmit antenna and is proportional to E_i. If

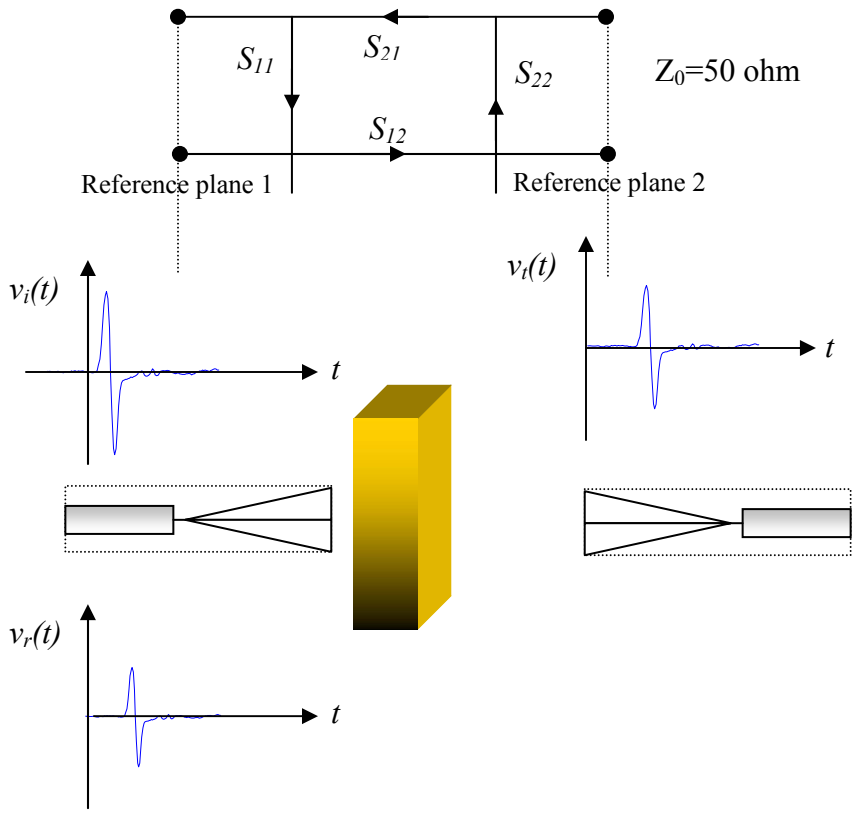

Figure 1. Incident, transmitted, and reflected waveforms observed in time-domain measurements.

the material slab is symmetric, then

$$S_{12}(j\omega) = S_{21}(j\omega)\,. \tag{10}$$

Instead of measuring the transmitted and received voltage signals, it is more convenient to measure the following two signals on the receive side:

- a transmit 'through' signal, $v_t(t)$, which is received with the material layer in place, and
- a free-space reference signal, $v_t^{fs}(t)$,which is the received signal without the layer.

Therefore, two measurements as illustrated in Figure 2 should be carried out with exactly the same distances and antenna setup. The free-space measurement is used as a reference to account for all the effects that are not due to the material under test; for example, the antennas, the receiver, and the signal generator. Assuming a fictitious layer of free-space of the same thickness as the material slab, the propagation through this layer involves simply a delay equals $\tau_0 \equiv d/c$, where d is the layer thickness and c is the speed of light in free space. In other words,

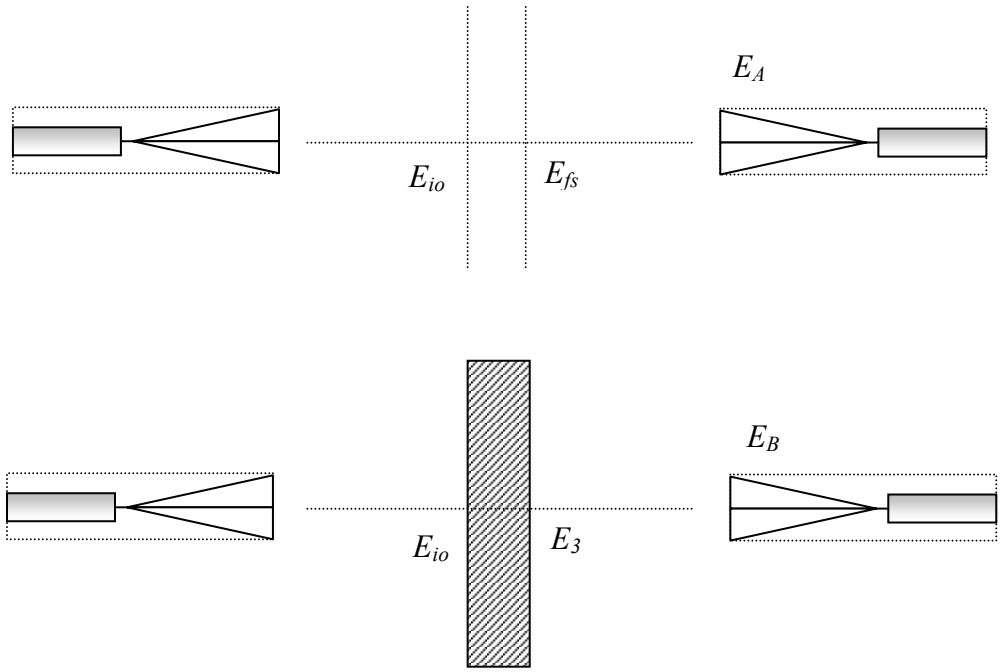

Figure 2. Two required measurements, without layer (free space) and with layer in place.

$$\frac{E_t^{fs}(j\omega)}{E_i(j\omega)} = e^{-j\omega\tau_0}. \tag{11}$$

The insertion transfer function is defined as the ratio of two radiation transfer functions,

$$H(j\omega) \equiv \frac{E_t(j\omega) \big/ E_i(j\omega)}{E_t^{fs}(j\omega) \big/ E_i(j\omega)} = \frac{E_t(j\omega)}{E_t^{fs}(j\omega)} = \frac{FFT(v_t(t))}{FFT(v_t^{fs}(t))} = \frac{V_t(j\omega)}{V_t^{fs}(j\omega)}. \tag{12}$$

Combining (9), (11), and (12), the scattering parameter S_{21} can be related to the insertion transfer function as

$$S_{21}(j\omega) = H(j\omega)e^{-j\omega\tau_0}. \tag{13}$$

In the frequency-domain method, the pulse signals are replaced with sinusoidal signals and a vector network analyzer is used to monitor the received waveforms. Otherwise, the measurement procedure is the same as that for the time-domain approach illustrated in Figure 2. Thus, in summary, first we measure the time-domain signal $v_t^{fs}(t)$ with a sampling oscilloscope or the frequency-domain signal $V_t^{fs}(j\omega)$ with a network analyzer in the absence of the material

layer. Then, we measure the time-domain signal $v_t(t)$ or the frequency-domain signal $V_t(j\omega)$ with the material layer in place. The insertion transfer function is then calculated using (12). Care must be taken to ensure that the conditions for the free-space measurement are as closely identical as possible to those for the measurement through the material slab. Once the insertion transfer function (or S_{21}) is obtained, numerical methods are used to extract the attenuation coefficient and dielectric constant of the material as detailed in the next section.

Using the time-domain waveforms, the delay between the two pulses can be measured to obtain an approximate value for the dielectric constant. The total signal power can also be measured in the free-space case and through the material to estimate the power loss due to propagation through the material. In the following sections, the procedure and signal processing required to extract the material parameters are discussed.

4 Analysis Techniques

The free-space and through-the-wall measurements would be most accurate if performed inside an anechoic chamber where all the multiplepath components and reflections from the floor and ceiling are absorbed. Ideally, the sample to be measured should be infinitely large to avoid scattering from the edges. Samples under test have to be at a far-field distance from the antenna, typically several meters for the frequency range of interest and the antenna dimensions. Maintaining these requirements is not a convenient task, keeping in mind that absorbers and chamber environment do not allow easy movements of large samples. Fortunately, time gating can be used to reduce significantly the undesired effects such as reflections from the surrounding walls and scattering from edges. For time gating to be efficient three conditions have to be met. First, the transmitter and the receiver antennas should be positioned away from the reflecting surfaces. Second, samples should have relatively large surface dimensions in order to minimize the edge effects. Finally, there should be flexibility in adjusting the distance between the antenna and the sample. Time gating can also be used to isolate a desired portion of the received signal; namely, the first single-pass of the signal transmitted through the slab. In this application, the sample thickness should be large enough to yield sufficient delay and thus allow zooming in and extracting the first pulse and removing all delayed pulses due to multiple reflections inside the slab. In the following subsections analysis techniques based on time-domain and frequency-domain measurements – single-pass, multiple-pass, and approximate solutions for low loss materials – are presented.

4.1 Single-Pass Technique

This technique can be used if the duration of the test pulse is sufficiently short or the wall or material slab under study has a thickness that is large enough to allow gating out the portions of the signal due to multiple reflections inside the slab.

A short-duration electromagnetic pulse, $E_i(t)$, is applied to a homogenous and isotropic material layer of thickness d. The transmitted signal, $E_t(t)$, results in a voltage at the receiver antenna terminals. To simplify the problem we assume that the wave is normally incident on the material surface and the duration of the pulse is smaller than the pulse travel time through the material. Then, multiple reflections inside the layer, which are delayed more than the pulse width, can be eliminated by means of time gating. The same technique can be used to eliminate antenna ringing and extraneous paths signal components. In summary, this is a single-pass duration-limited transient measurement procedure based on a one-dimensional model of plane-wave propagation through a planar layer.

The derivations pertaining to the short-pulse propagation measurements are available in [Aur96]. The results are summarized below.

$$\varepsilon_r(f) \cong \left[1+\frac{\Delta\tau(f)}{\tau_0}\right]^2 = \left[1-\frac{1}{2\pi\tau_0}\frac{d\Phi_{sp}(f)}{df}\right]^2, \tag{14}$$

$$p_e(f) \cong -\frac{1}{\pi f \tau_0 \sqrt{\varepsilon_r(f)}} \ln\left[\frac{\left[1+\sqrt{\varepsilon_r(f)}\right]^2}{4\sqrt{\varepsilon_r(f)}}\left|H_{sp}(f)\right|\right], \tag{15}$$

where $H_{sp}(f) = |H_{sp}(f)| \exp[j\Phi_{sp}(f)]$ is the single-pass insertion transfer function. It is the ratio of the Fourier transform of the single-pass received signal when the slab is in place to the Fourier transform of the single-pass received signal in the absence of slab. It should be noted that the derivative term $d\Phi_{sp}(f)/df$ in (14) is based on the assumption that the phase varies linearly with frequency. The advantage of using the derivative of the phase is to avoid tracking the unwrapped phase function. As a function of the unwrapped phase, the dielectric constant is given by

$$\varepsilon_r(f) \cong \left[1+\frac{\Delta\tau(f)}{\tau_0}\right]^2 = \left[1-\frac{\Phi_{sp}(f)}{2\pi\tau_0 f}\right]^2. \tag{16}$$

4.2 Multiple-Pass Technique

If single-pass signal cannot be gated out satisfactorily, multiple reflections from the slab interior that constitute part of the received signal must be accounted for. This situation particularly arises when the transit time through the thickness of the slab is small compared to the pulse duration. In this case, an insertion transfer function that accounts for multiple reflections is needed. This insertion transfer function, denoted as $H(j\omega)$, has a definition similar to H_{sp} except that single-pass signals should be replaced with signals containing all multiple-pass components in the Fourier transform calculations. Thus, time-domain measured data can be used to find $H(j\omega)$. However, $H(j\omega)$ can be conveniently calculated using a frequency-domain technique. In this method, measured data are obtained using a sweep generator and a vector network analyzer. For frequency-domain measurements too, ideally the slab has to be infinitely large and should be measured in an anechoic chamber in order to avoid capturing the scattering from the edges of slab and reflections from the floor, ceiling, and adjacent walls. However, if the undesired scattering and reflection signals can be removed through time gating mechanisms,as explained later, the signal received in a relatively large time window provides sufficiently accurate results.

In order to obtain an expression for the insertion transfer function $H(j\omega)$, let us assume that an *x*-polarized uniform plane-wave, representing the local far-field of a transmit antenna is normally incident on a slab of material of thickness *d*. The material has an unknown complex dielectric constant $\varepsilon_r = \varepsilon_r' - j\varepsilon_r''$. The incident plane-wave, as depicted in Figure 3, establishes a reflected wave in region I (air), a set of forward and backward traveling waves in region II (material), and a transmitted wave in region III (air). The electric and the magnetic fields in region I can be written as

$$\vec{E}_1 = \hat{a}_x (E_{i0} e^{-j\beta_0 z} + E_{r0} e^{+j\beta_0 z}), \tag{17}$$

$$\vec{H}_1 = \hat{a}_y \frac{1}{\eta_1} (E_{i0} e^{-j\beta_0 z} - E_{r0} e^{+j\beta_0 z}), \tag{18}$$

where $\beta_0 = \omega\sqrt{\mu_0\varepsilon_0} = \frac{2\pi}{\lambda} = \frac{2\pi f}{c}$ and $\eta_1 = \sqrt{\frac{\mu_0}{\varepsilon_0}} = 120\pi\Omega$.

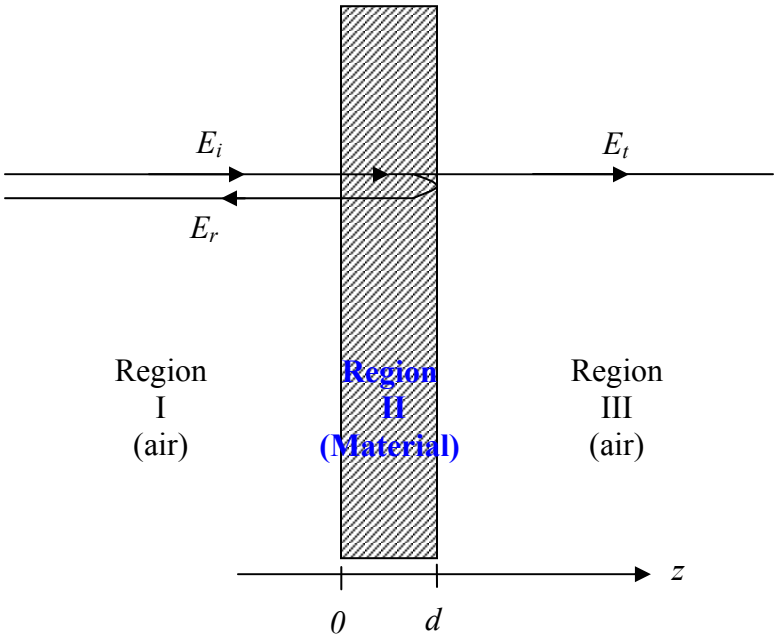

Figure 3. Electromagnetic Plane-Wave Propagation through a slab.

In region II, the fields are given by

$$\vec{E}_2 = \hat{a}_x (E_2^+ e^{-\gamma z} + E_2^- e^{+\gamma z}), \tag{19}$$

$$\vec{H}_2 = \hat{a}_y \frac{1}{\eta_2} (E_2^+ e^{-\gamma z} - E_2^- e^{+\gamma z}), \tag{20}$$

where $\gamma = \alpha + j\beta = j\omega\sqrt{\mu_0 \varepsilon_0 (\varepsilon_r' - j\varepsilon_r'')}$ and $\eta_2 = \sqrt{\dfrac{\mu}{\varepsilon_0 (\varepsilon_r' - j\varepsilon_r'')}}$. Similarly, in region III the fields are expressed as

$$\vec{E}_3 = \hat{a}_x E_3^+ e^{-j\beta_0 z}, \tag{21}$$

$$\vec{H}_3 = \hat{a}_y \frac{1}{\eta_1} E_3^+ e^{-j\beta_0 z}. \tag{22}$$

Boundary conditions require continuity of the tangential components of the $\vec{E}$ and $\vec{H}$ fields at z=0 and z=d. These conditions are summarized as

$$E_1(0) = E_2(0) \Rightarrow E_{i0} + E_{r0} = E_2^+ + E_2^-, \tag{23}$$

$$H_1(0) = H_2(0) \Rightarrow E_{i0} - E_{r0} = \frac{\eta_1}{\eta_2}(E_2^+ - E_2^-), \tag{24}$$

$$E_2(d) = E_3(d) \Rightarrow E_2^+ e^{-\gamma d} + E_2^- e^{+\gamma d} = E_3^+ e^{-j\beta_0 d}, \tag{25}$$

$$H_2(d) = H_3(d) \Rightarrow E_2^+ e^{-\gamma d} - E_2^- e^{+\gamma d} = \frac{\eta_2}{\eta_1} E_3^+ e^{-j\beta_0 d}. \tag{26}$$

We need to find $T=\frac{E_3^+ e^{-j\beta_0 d}}{E_{i0}}$ which is equivalent to S_{21} in the scattering parameters terminology.

Manipulating the boundary conditions, we obtain

$$(23)+(24) \Rightarrow 2E_{i0} = E_2^+(1+\frac{\eta_1}{\eta_2}) + E_2^-(1-\frac{\eta_1}{\eta_2}), \tag{27}$$

$$(25)+(26) \Rightarrow 2E_2^+ e^{-\gamma d} = E_3^+ e^{-j\beta_0 d}(1+\frac{\eta_2}{\eta_1}), \tag{28}$$

$$(25)-(26) \Rightarrow 2E_2^- e^{+\gamma d} = E_3^+ e^{-j\beta_0 d}(1-\frac{\eta_2}{\eta_1}). \tag{29}$$

Substituting for E_2^+ from (28) and for E_2^- from (29) into (27) yields,

$$2E_{i0} = \frac{1}{2}E_3^+ e^{(+\gamma - j\beta_0)d}(1+\frac{\eta_2}{\eta_1})(1+\frac{\eta_1}{\eta_2}) + \frac{1}{2}E_3^+ e^{(-\gamma - j\beta_0)d}(1-\frac{\eta_2}{\eta_1})(1-\frac{\eta_1}{\eta_2}). \tag{30}$$

The transmission coefficient is now readily obtained as

$$T = \frac{E_3^+ e^{-j\beta_0 d}}{E_{i0}} = \frac{4}{e^{\gamma d}\left(2+\frac{\eta_1}{\eta_2}+\frac{\eta_2}{\eta_1}\right) + e^{-\gamma d}\left(2-\frac{\eta_1}{\eta_2}-\frac{\eta_2}{\eta_1}\right)} \tag{31}$$

Based on the definition of the insertion transfer function given in (12), we can write

$$\frac{E_B}{E_A} = \frac{E_3/E_{oi}}{E_{fs}/E_{oi}} = \frac{T}{e^{-j\beta_0 d}} = Te^{j\beta_0 d} = H(j\omega). \tag{32}$$

Thus,

$$H(j\omega) = \frac{4e^{j\beta_0 d}}{e^{\gamma d}(2+\frac{\eta_1}{\eta_2}+\frac{\eta_2}{\eta_1}) + e^{-\gamma d}(2-\frac{\eta_1}{\eta_2}-\frac{\eta_2}{\eta_1})}. \tag{33}$$

4.2.1 Exact Solution

When the complex insertion transfer function $H(j\omega)$ is determined by measurements as described in Section 3, equation (33) can be solved for the complex dielectric constant $\varepsilon_r = \varepsilon_r' - j\varepsilon_r''$. In terms of the scattering parameter S_{21}, the parameter that is directly measured, (33) with the help of (13) can be easily cast into the following form [Alq96],

$$\left(x + \frac{1}{x}\right)\sinh(xP) + 2\cosh(xP) - \frac{2}{S_{21}} = 0\,, \tag{34}$$

where $x = \sqrt{\varepsilon_r}$ and $P = j\beta_0 d$. An alternative derivation of (34) based on bounce diagram is presented in Appendix A1. This equation can be solved numerically using two-dimensional search algorithms. The convergence of this algorithm is not always guaranteed taking into account possible multiple solutions and noise in the measurements. In the next section, using reasonable assumptions, (33) is reduced to a one-dimensional problem involving real equations only.

4.2.2 Approximate Solution

When the material occupying region II is low loss, $\varepsilon_r''/\varepsilon_r' << 1$ and the following approximations can be used,

$$\gamma = \alpha + j\beta = j\omega\sqrt{\mu_0\varepsilon_0(\varepsilon_r' - j\varepsilon_r'')} \cong j\omega\sqrt{\mu_0\varepsilon_0}\sqrt{\varepsilon_r}\,(1 - j\frac{1}{2}\frac{\varepsilon_r''}{\varepsilon_r'})$$

$$= j\beta_0\sqrt{\varepsilon_r'}\,(1 - j\frac{1}{2}\frac{\varepsilon_r''}{\varepsilon_r'})$$

and

$$\eta_2 = \sqrt{\frac{\mu}{\varepsilon_0(\varepsilon_r' - j\varepsilon_r'')}} \cong \sqrt{\frac{\mu_0}{\varepsilon_0\varepsilon_r'}} = \frac{\eta_1}{\sqrt{\varepsilon_r'}}\,.$$

Then, $\frac{\eta_1}{\eta_2} + \frac{\eta_2}{\eta_1} \cong \sqrt{\varepsilon_r'} + \frac{1}{\sqrt{\varepsilon_r'}} = \frac{\varepsilon_r' + 1}{\sqrt{\varepsilon_r'}}$ and (33) reduces to

$$H(j\omega) = \frac{4e^{j\beta_0 d}}{e^{(\alpha+j\beta)d}\left(2+\frac{\varepsilon_r'+1}{\sqrt{\varepsilon_r'}}\right)+e^{-(\alpha+j\beta)d}\left(2-\frac{\varepsilon_r'+1}{\sqrt{\varepsilon_r'}}\right)}. \tag{35}$$

Rewriting the insertion transfer function in terms of magnitude and phase, we obtain

$$\left|H(j\omega)\right| = \left(\frac{16}{e^{2\alpha d}\left(2+\frac{\varepsilon_r'+1}{\sqrt{\varepsilon_r'}}\right)^2+e^{-2\alpha d}\left(2-\frac{\varepsilon_r'+1}{\sqrt{\varepsilon_r'}}\right)^2+2\cos(2\beta d)\left(4-\left(\frac{\varepsilon_r'+1}{\sqrt{\varepsilon_r'}}\right)^2\right)}\right)^{1/2} \tag{36}$$

and

$$\angle H(j\omega) = \beta_0 d - \phi \tag{37}$$

where

$$\phi = \tan^{-1}\left\{\left[\frac{e^{\alpha d}\left(2+\frac{\varepsilon_r'+1}{\sqrt{\varepsilon_r'}}\right)-e^{-\alpha d}\left(2-\frac{\varepsilon_r'+1}{\sqrt{\varepsilon_r'}}\right)}{e^{\alpha d}\left(2+\frac{\varepsilon_r'+1}{\sqrt{\varepsilon_r'}}\right)+e^{-\alpha d}\left(2-\frac{\varepsilon_r'+1}{\sqrt{\varepsilon_r'}}\right)}\right]\cdot\tan(\beta d)\right\}. \tag{38}$$

Equation (38) can be written in a more compact form as

$$\phi = \tan^{-1}\left\{\left[\frac{1-e^{-2\alpha d}Q}{1+e^{-2\alpha d}Q}\right]\cdot\tan(\beta d)\right\} \tag{39}$$

where

$$Q = \frac{2-\frac{\varepsilon_r'+1}{\sqrt{\varepsilon_r'}}}{2+\frac{\varepsilon_r'+1}{\sqrt{\varepsilon_r'}}} = \frac{2\sqrt{\varepsilon_r'}-\varepsilon_r'-1}{2\sqrt{\varepsilon_r'}+\varepsilon_r'+1} = -\frac{(\sqrt{\varepsilon_r'}-1)^2}{(\sqrt{\varepsilon_r'}+1)^2} = -\left(\frac{\sqrt{\varepsilon_r'}-1}{\sqrt{\varepsilon_r'}+1}\right)^2. \tag{40}$$

For most applications of interest Q has a small value. For example, for the relative permittivities of 2.0, 4.0, and 8.0, Q is about 0.02, 0.1, and 0.3, respectively. Later we will use this fact to further simplify the solution. For the time being no assumption is made about Q. Letting $e^{-2\alpha d} = X$, then

$$|H(j\omega)|^2 = \frac{16\varepsilon_r'}{\frac{1}{X}\left(\sqrt{\varepsilon_r'}+1\right)^4 + X\left(\sqrt{\varepsilon_r'}-1\right)^4 - 2\cos(2\beta d)\left(\varepsilon_r'-1\right)^2}, \tag{41}$$

or

$$X^2\left(\sqrt{\varepsilon_r'}-1\right)^4 - 2\left[\cos(2\beta d)\left(\varepsilon_r'-1\right)^2 + 8\frac{\varepsilon_r'}{|H(j\omega)|^2}\right]X + \left(\sqrt{\varepsilon_r'}+1\right)^4 = 0,$$

which is a quadratic equation in terms of X. Solving this equation or X, we have

$$X = e^{-2\alpha d} = \frac{\left[\cos(2\beta d)\left(\varepsilon_r'-1\right)^2 + 8\frac{\varepsilon_r'}{|H(j\omega)|^2}\right] \pm \sqrt{\left[\cos(2\beta d)\left(\varepsilon_r'-1\right)^2 + 8\frac{\varepsilon_r'}{|H(j\omega)|^2}\right]^2 - \left(\varepsilon_r'-1\right)^4}}{\left(\sqrt{\varepsilon_r'}-1\right)^4} \tag{42}$$

Only the solution with negative sign in (42) is valid (the proof is given in Appendix A2. Substituting for X from (42) in the phase expression (39), we obtain the following equation which is only in terms of ε_r'.

$$\tan\left[\beta_0 d - \angle H(j\omega)\right] + \frac{1-QX}{1+QX}\tan(\beta d) = 0 \tag{43}$$

Solving this equation numerically, ε_r' is readily determined. Then, X and subsequently α are found from (42). Finally, ε_r'' is calculated using

$$\varepsilon_r'' = \frac{2c\alpha\sqrt{\varepsilon_r'}}{\omega}. \tag{44}$$

4.2.2.1 Special Case

If it can be further assumed that $e^{-2\alpha d} << 1$, then

$$\phi \approx \tan^{-1}(\tan(\beta d)) = \beta d$$

and

$\angle H(j\omega) = \beta_0 d - \beta d = \beta_0 d - \beta_0 d\sqrt{\varepsilon_r'}$, where $\beta \approx \beta_0\sqrt{\varepsilon_r'}$ and

$$\varepsilon_r' = \left(\frac{\beta_0 d - \angle H(j\omega)}{\beta_0 d}\right)^2 = \left(1 - \frac{\angle H(j\omega)}{\beta_0 d}\right)^2. \tag{45}$$

Once ε_r' is determined, α and then ε_r'' can be found from $|H(j\omega)|^2$ using the following relationships,

$$|H(j\omega)|^2 \approx \frac{16}{e^{2\alpha d}\left(2+\frac{\varepsilon_r'+1}{\sqrt{\varepsilon_r'}}\right)^2 + 2\cos(2\beta d)\left[4-\left(\frac{\varepsilon_r'+1}{\sqrt{\varepsilon_r'}}\right)^2\right]} \tag{46}$$

$$\alpha = \frac{1}{2d}\ln\left\{\frac{\frac{16}{|H(j\omega)|^2} + 2\cos(\beta d)\left[\frac{(\varepsilon_r'-1)^2}{\varepsilon_r'}\right]}{\frac{(\sqrt{\varepsilon_r'}+1)^4}{\varepsilon_r'}}\right\}. \tag{47}$$

This simplified analysis reduces to the single pass case as in [Aur96], where the wall is assumed to be thick and single transmitted pulse can be time gated. This is because the assumption $e^{-2\alpha d} << 1$ has the implication that the multiple-pass components of the received signal are very small, as for $\alpha d >> 1$ these components are attenuated significantly more than the single-pass signal.

5 Comparison of Various Techniques

In section (4.1) two sets of expressions for the calculation of dielectric constant and loss tangent, based on single-pass insertion transfer function $H_{sp}(f)$, were presented. These are equations (14) and (15) for single-pass involving phase derivative, and equations (16) and (15) for single-pass involving the phase itself. Similarly, in section (4.2) two sets of expressions for the calculation of dielectric constant and loss tangent or attenuation coefficient, based on multiple-pass insertion transfer function $H(j\omega)$, were presented. These are equations (34) or (35) for exact solutions (material need not be assumed low loss), and equations (42), (43), and (44) for approximate solutions applicable to low loss materials. Here, the results obtained from all four sets of solutions are calculated and compared in order to better appreciate the accuracy as well as the applicability of each method. Measurements are carried out for a sample wooden door representing the slab. The results for the dielectric constant obtained from the four sets of solutions mentioned above are shown in Figure 4. It is noted that, with exception of single-pass phase derivative method, the results from other three solutions are in excellent agreement. This agreement is due to the fact that for this specific sample (wooden door), multiple reflections

inside the door are very small compared to the first single-pass. It is further noted that the results obtained from the exact and approximate solutions (multiple-pass) are nearly identical, indicating that the door material is low loss. The small difference between the exact and approximate results might be attributed to the termination criteria of the search algorithms. The fact that the search for a complex solution problem can be reduced to a one-dimensional problem is illustrated in Figure 5. This figure illustrates that the complex search problem is separable, as any cut on a constant ε_r'' plane results in the same minimum.

Both the exact complex and approximate real equations have spurious solutions that can be avoided by starting with an initial guess obtained from the single-pass solution at a high frequency and by using a constrained search. At high frequencies the wavelength is smaller and the assumption of thick slab become more reasonable. The solution obtained at a high frequency point is then used as an initial guess for the next frequency point, because variations of the dielectric constant versus frequency are slow over a narrow frequency range.

Whenever single-pass time gating is possible, the single-pass analysis technique can be used. Using time-domain measurements, this technique is applicable if one of the following two requirements is met: (i) the pulse has a width shorter than the transit time through the slab, (ii) the material has a sufficiently high loss so that the second and higher-order reflections are attenuated much more than the first single-pass signal. If single-pass time gating is not possible, the multiple-pass analysis technique should be used. First the approximate solution is attempted, but the result has to be validated by comparing with the exact solution to see if the low loss requirement is met. Whenever possible, the results from both time-domain and frequency-domain measurements should be obtained and compared to ensure the validity of measurements and also avoid any spurious results.

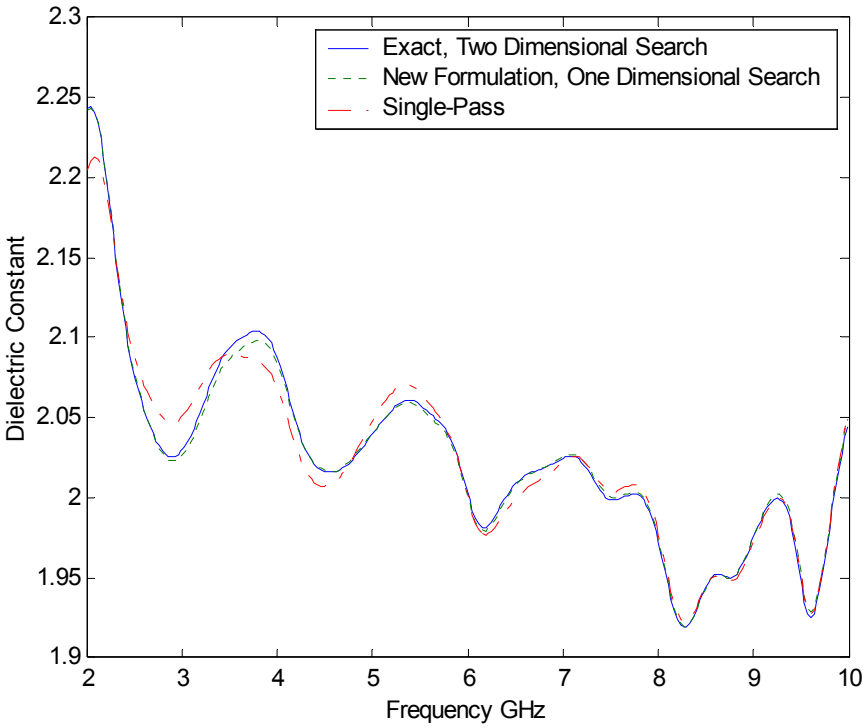

Figure 4. Comparison between the different measurement and analysis techniques.

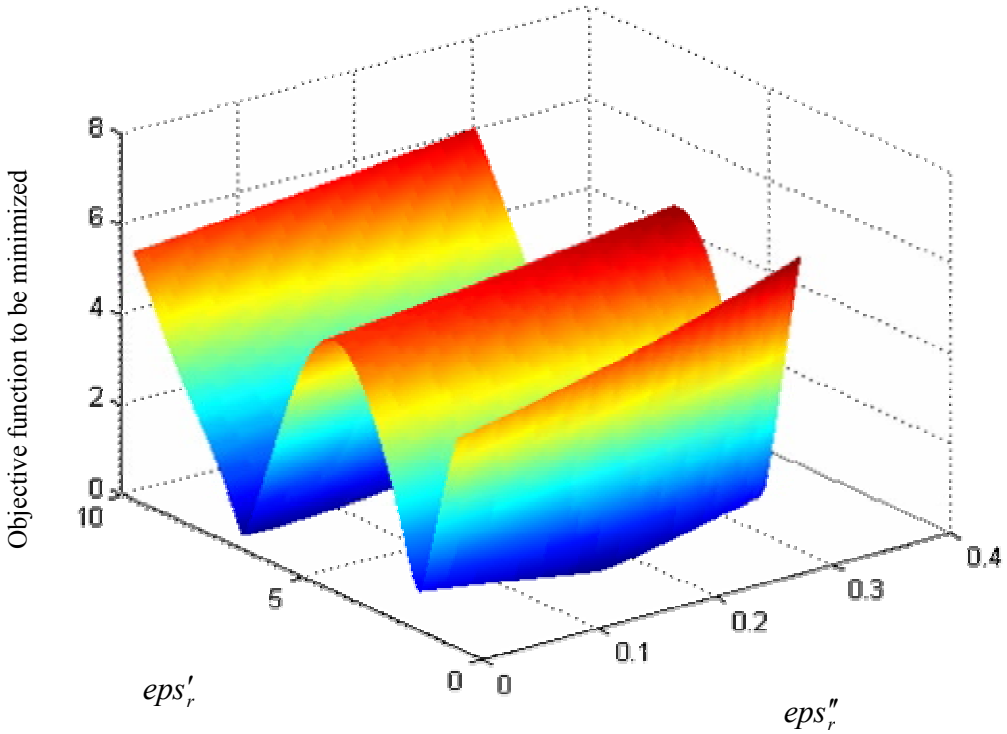

Figure 5. Two-dimensional search example, illustrating the possibility of reducing it to a one-dimensional search.

6 Signal Processing and Parameters Extraction

In this section, the procedure for processing the measured data and extracting the material parameters is presented. The procedure is summarized in the flowchart shown in Figure B1-1. Plots illustrating the variations of parameters versus frequency for various materials are provided in Appendix B1 and will be further discussed in later sections. As mentioned earlier, two measurements are performed; the first is the "free-space reference" in the absence of the material, while the second is the "through" measurement that is performed with the material in place. Measurements are carried out in both the frequency and time domains. Transformations between the two domains are possible by means of Fourier or inverse Fourier transform.

6.1 Data Acquisition

Frequency-domain measurements can be made in a frequency range from 45 MHz to 15 GHz. Over a given frequency range 801 complex data points (magnitude and phase) can be collected which is the maximum number of points allowed by the network analyzer. This limitation on the number of points imposes a limit on measurements resolution and the accuracy of transformation to time domain using inverse Fourier transform. A low-pass finite-impulse-response (FIR) filter is used to remove the noise beyond the antenna bandwidth. The cutoff frequencies of the filter are adjusted to remove the noise regions. The order of the filter is chosen to be 100. A sample frequency measurement is shown in Figure B1-2 which illustrates the magnitude and the unwrapped phase of the 'free-space' and 'through' signals, the FIR filter characteristic, and the obtained impulse responses. Zeros are padded to get higher resolution in the transformed time domain.

For time-domain measurements, 128 traces are averaged and acquired in a 5ps sampling time using the sampling oscilloscope. Offset adjustment is achieved through load calibration and post-processing. The signal acquiring window spans more than 10ns and consists of 2048 points. An illustrative measurement is shown in Figure B1-3(a).

6.2 Time Delay and Initial Guess for Permittivity

The 'through' and 'free-space' time-domain measured signals or the corresponding impulse responses obtained from frequency-domain measurements are correlated using a sliding correlator to obtain the first guess on the delay and effective dielectric constant. The shape of the correlator is illustrated in Figure B1-3b. An estimate of the average dielectric constant could also be obtained through peak-to-peak impulse time delay, $\Delta\tau$. An average value of the dielectric constant that does not reflect the frequency dependence is given by

$$\varepsilon_r' \cong \left[1+\frac{\Delta\tau}{d/c}\right]^2, \tag{48}$$

where d is the thickness of the slab and c is the speed of light in free-space.

6.3 Time Gating

Time gating is required to remove multi-pass components in received signals, as they are not accounted for in the calculation and extraction of material parameters. Multiple reflections should be gated out too if single-pass technique is used. In multiple-pass technique, perfect time gating cannot be achieved because, strictly speaking, infinite acquisition time is required to capture infinite number of multiple reflections. However, because higher-order multiple reflections die out quickly for materials of interest in this research, satisfactory time gating is still achievable.

Time gating capabilities are enhanced with shorter pulse durations and longer distances between the test material and reflectors and scatterers. If single-pass is desired, pulse duration should be shorter than the twice the travel time through the slab to avoid pulse overlapping.

To avoid abrupt changes on the signal level, the gating-window should have smooth transition from zero to the flat level. This window is based on the modified Kaiser window with a flat region in the middle. However, the results for material parameters should be essentially independent of the used window. Various parameters of the window are changed to make sure that the results are not sensitive to the details of the window. A Kaiser window of length M has a time domain sequence $h(n)$ given by,

$$\frac{I_0\left[\alpha_0\sqrt{\left(\frac{M-1}{2}\right)^2-\left(n-\frac{M-1}{2}\right)^2}\right]}{I_0\left[\alpha_0\left(\frac{M-1}{2}\right)\right]}, \qquad 0\le n\le M-1, \tag{49}$$

where I_0 is the modified Bessel function of order zero and α_0 is a design smoothing factor set equal to 25. The window size was chosen to be 2ns for source#1, 0.5ns for source#2, and 3ns for the Fourier-transformed data measured with the network analyzer. These values were chosen to allow for nearly optimum time gating. The windows have two symmetrical transition regions and a flat region defined by the intervals (0.2,1.6,0.2), (0.1,0.3,0.1), and (1,1,1) ns, –parameters within parantheses refer to (risetime, width of flat region, fall time), respectively – as illustrated in Figure 6.

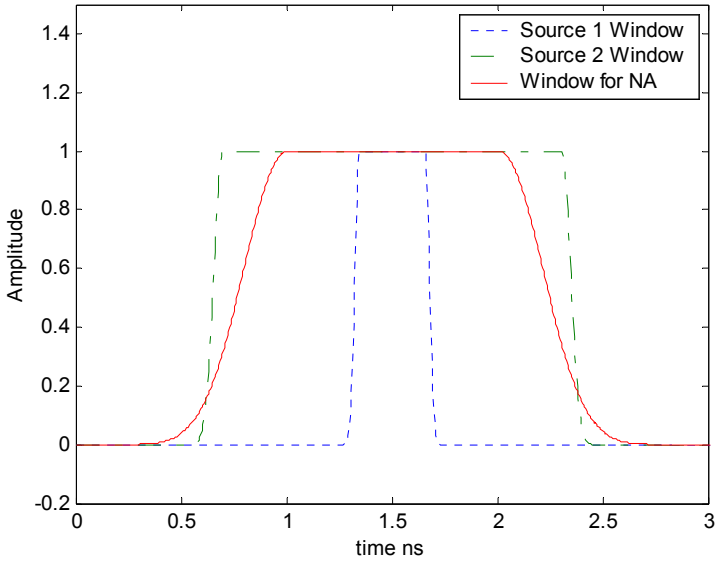

Figure 6. Three different time domain gating windows.

If the 'through' and 'free-space' signals both return to the zero level in the window, the gating can be implemented easily. If the signal does not become exactly zero in the window, the window opening for the received signal is delayed by an amount equal to τ_0. After time gating the signals with proper zero padding, the fast Fourier transform (FFT) and (12) are used to calculate the insertion transfer function.

6.4 Propagation and Material Parameters

Form the complex insertion transfer function, the dielectric constant and loss tangent of the material under test can be extracted. Table 1 summarizes the analysis techniques and the corresponding equations required to extract the material parameters. The choice of the analysis technique is based on how satisfactorily time gating can be implemented. In many cases, multiple reflections inside the slab decay rapidly so that single-pass or multiple-pass techniques essentially yield the same results.

Six different measurements are performed for the characterization of each material. These include four time-domain measurements, with two different pairs of antennas and two pulse generators, and two frequency-domain measurements using two pairs of antennas. The results for six different time-gated measurements for the sample door are given in Figure B1-4.

Table 1 Summary of analysis techniques and required equations

Analysis Technique	Equations
Single-Pass (low -loss)	(14), (15)
Multiple-pass (exact solution)	(34) or (35)
Multiple-pass (approximate solution, low-loss)	(42), (43), (44)

The parameters for other materials that have been tested are given in Figure B1-5. The confidence on the obtained result is strengthened when the time-domain and frequency-domain measurements agree, because different equipments, calibrations, and processes are involved. There are two advantages for the frequency-domain method, one is that characterization over a higher frequency range can be achieved by using multi-band filters, and another advantage is that no external synchronization is required. Both input and output are centrally processed, thus reducing the synchronization errors. On the other hand, the time-domain method offers higher resolution and more data points. Examining Figure B1-5 reveals that the time-domain measurements performed with short pulses (source #2) exhibit less variations than the frequency-domain results across the frequency band of interest.

7 Description of Samples and Wall Materials

Ten different wall materials commonly encountered in building environments are selected for UWB characterization. These include drywall, glass, wallboard, styrofoam, cloth office partition, wooden sample door, wood, structure wood, brick, concrete block, and reinforced concrete column. Table 2 lists the selected samples and their dimensions. Thickness measurements are taken as an average of 6 to 8 repeated measurements for best accuracy.

Table 1: Materials, sample dimensions, and parameters at 5GHz

Material	Dimensions (cm)	ε_r	Loss at 5 *GHz (dB)*
Wallboard (drywall)	**1.16992** x 121.8 x 196.9	2.44	0.45
Cloth Partition	**5.9309** x 140.7 x 153.1	1.23	2.55
Structure Wood	**2.06781** x 121.5 x 197.8	2.11	1.35
Sample door	**4.44754** x 90.70 x 211.8	2.08	2.0
Ply Wood	**1.52146** x 121.9 x 197.51	2.49	1.75
Glass	**0.235661** x 1.44 x 111.76	6.40	1.25
Styrofoam	**9.90702** x 121.8 x 197.7	1.11	0.10
Bricks (single)	**8.71474** x 5.82676 x 19.8	4.22	6.45
Concrete Block	**19.45** x 39.7 x 19.5	2.22	13.60
Reinforced Concrete (TDL)	**60.96** x 121.92 x …	-	-

Note: The first number in the dimensions column is the thickness of the sample; i.e. the propagation path length through the material.

The requirement that 'free-space' and 'through' measurements should be performed with the same antenna spacings, makes in-*situ* measurements very difficult. After the in-*situ* 'through' measurements are performed, the 'free-space' measurements should be made at a different location but with the same distance between the transmiting and receiving antennas as in the 'through' measurement setup. Since it is impossible to have exactly the same distances between the antennas for measurement setups at two different locations, errors will inevitably result in the calculation of insertion transfer function. For example, at 10GHz the wavelength is about 3cm, then1mm change in the spacing between the two antennas results in 12 degrees phase error. This is an extremely tight tolerance requirement that cannot be met easily. To overcome this problem, a moving platform was constructed, and bricks and blocks were used to build walls on it. This allows us to move the wall between the two antennas and make repeated measurements while the setup is kept at a fixed location. Figure B3-1 illustrates the brick and block samples, moving walls built with bricks, blocks, and styrofoam. Styrofoam slabs are used to secure the walls on the platform. One styrofoam slab was also measured to estimate its loss and dielectric constant and hence its impact on the measurement of other materials. It has very low loss and a dielectric constant close to unity, thus it can be assumed to be effectively 'air'.

A reinforced concrete pillar in the 3rd floor of Whittemore Hall, the building that houses the Electrical Engineering Department of Virginia Tech, was also measured. A reinforced pillar in the Time Domain Lab (TDL) was also measured.

The cloth office partitions that were tested have round edges at the upper ends with wooden caps for holding the cloth material tight. Each partition has two metal stands and as well as support pieces inside. Figure B3-2 shows the different materials and walls used in measurements.

8 Measurement Results

The dielectric constant and the loss at 5 GHz as representative values of parameters for the selected materials are listed in Table 2. The 5-GHz frequency is in a region of bandwidth where the measurements are believed to be most accurate, because the results obtained from different techniques agree very well and the amount of power transmitted in this region is significantly far above the noise floor. It is emphasized that for most materials measuring the loss is more difficult than measuring the real part of effective permittivity [Gey90]. A straight line is used to model the insertion loss versus frequency [Gib99]. The fitted insertion transfer functions for different materials are shown in Figure B2-1. The insertion transfer function for the door is re-plotted in part (b) of Figure B2-1 for ease of comparison. Cloth partition shows higher loss due to support elements inside the partitions. Similarly, the dielectric constants are presented in Figure B2-2. The results for the brick wall and the concrete block wall are over smaller bandwidths because of higher losses of these materials that reduce their useful bandwidths. The dielectric constant versus frequency can be modeled as a straight line with very small negative slop. However, the dielectric constant for the brick has a small positive slope that is believed to be due to the non-homogeneity of the sample. Attenuation constants for the door, wood, and structure wood sample are given in Figure B2-3. It was possible to extract the attenuation constant for these materials due to their moderate loss.

To gain more insight into the effects of various walls on the propagation of UWB pulses, the ‘free-space’ and ‘through’ gated signals for all the measured materials are presented in Figures B2-4 through B2-9. For the case of blocks and bricks, the un-gated signals are presented due to the difficulty of gating.

The dielectric constant of the glass sample could not be measured using the time delay between peaks of the received pulses and the single-pass technique. This is because of the small thickness of the glass that does not allow multiple reflections to be avoided, thus the multiple-pass analysis should be used.

The reinforced concrete wall resulted in a very small amount of received power. No further processing could be done, but an average dielectric constant was obtained by measuring the time delay between the incident and received pulses. For better viewing, a longer time window is shown in Figure B2-9. This figure illustrates multiple reflections inside the reinforced concrete pillar. It is important to note that this window includes multi-pass components that might not travel through the pillar. A repeated 'W' shape is observed in the receiver signal. For reinforced concrete, concrete block, and brick walls, a 10 dB gain and15 GHz bandwidth amplifier was used at the receiver side to increase the measured signal level.

9 Related Issues

In the following section, some points related to validity of the measurements are discussed. These include distance between the samples and antennas, slab thickness and multi-layer study, repeatability, and variability.

9.1 Distance from the Sample

The distance between a sample and the antenna should be long enough to ensure that the sample is in the far field of the antenna. On the other hand, as the sample is moved away from the antenna, edge and scattering effects cannot be gated out. Hence, a trade-off has to be made without degrading the results. Moreover, as the distance increases the signal level decreases and hence the frequency range over which reliable characterization can be made becomes smaller. Most of our measurements were performed with a total distance of 1-3 meters. However, the effect of the distance would not be pronounced if the 'free-space' and 'through' measurements are carried out with exactly the same setup. An experiment was done by varying the distance between the antennas and the sample in steps of 0.25m. No significant change was observed other than the signal level.

9.2 Wall Thickness and Multi-layer Study

The thickness of the layer under study is critical to the measurement outcomes. If the thickness is very small error becomes more pronounced. For example, to estimate the dielectric constant of a slab of glass with 2mm thickness, we should be able to measure the delay as result of passing through this thin layer. If the thickness is larger, there will be a larger delay to measure and hence less relative error in the thickness of the layer. On the other hand, very thick slabs may cause high losses, resulting in weak signal levels that cannot be accurately measured. For the case of glass sample, slabs consisting of one, two, and three layers were tested to confirm the obtained parameters. The layers were carefully aligned to reduce the air gap. For the case of the board, two layers were tested to confirm the results.

9.3 Repeatability Analysis

Repeatability analysis describes the process of evaluating the precision of measurements taken at different instances of time. Measurements that have high precision are said to be repeatable [Yoh01]. One important factor is to allow the equipments to warm up for a stable performance. There is a small drift in the pulse with respect to the time axis when the equipment warms up. Figures B2-10, and B2-11 illustrate the repeatability of the frequency and time-domain measurements, respectively. Three different measurements of the wallboard sample are shown. The wallboard was chosen as they have smaller thickness and low loss compared with other materials. Examining the plots of insertion transfer functions and dielectric constants and noting that the differences in the measurement results are minor lead to the conclusion that the measurements are repeatable. The differences noticed in the plots must include tolerances of the measurement setup.

9.4 Variability Analysis

Variability analysis describes the process of evaluating the precision of measurements of different samples of the same material. Different measurements of different samples that have high precision are said to have low variability. In the case of wall measurements, two different samples of two different wallboards were measured (using the same calibration). The results of these measurements are given in Figures B2-10 and B2-11. It should be noted that the results for both repeatability and variability analyses are shown on the same plots. Examining these plots and noting the differences in the measurement results are minor lead to the conclusion that the two wallboards have a low variability, yet the differences indicate that there is some degree of variability in the walls. In indoor environments, wallboards built from different materials and by different manufacturers are used. But, this should not be a concern as the primary objective of the material/wall characterization effort is to obtain estimates of the loss and the associated delay for different construction materials and gain insights into how UWB propagation is affected by these materials.

10 Remarks on Pulse Shaping, UWB Receiver Design, and Modeling Hints

The following section is dedicated to putting the results of measurements into perspective with regard to receiver design, pulse shaping, and channel modeling.

10.1 Receiver Design and Pulse Shaping

The idea of using correlators at the receiver might not work very well in a non-line-of-site configuration. The pulse seems to undergo shape deformation as it propagates through structures with small dimension due to inter-pulse interferences. Multiple reflections within the

material and multipath components have a significant impact on the maximum data rate and/or multiple access capabilities of UWB systems. The claim that UWB has high multipath resolution works very well in a free-space line-of-site configuration but seems to be less certain in structures with fine details relative to the pulse duration.

Two seemingly contradicting requirements have to be traded off. One would like to have the pulse with very short duration and at the same time to have enough low frequency components. As the pulse gets shorter, its spectral contents are shifted to higher frequencies which suffer more attenuation as the pulse propagates. When deciding on the spectrum to be used, it is important to note that as the signal is shift to higher frequencies, the original reasons for proposing UWB including spectrum reuse and propagation through-the-wall become irrelevant. Reception based on pulse shape might not be the best approach for indoor environments. Other means of capturing the signal energy might prove to be more practical.

The originally proposed modulation scheme, in which a bit is demodulated as a 'zero' or 'one' based on the time delay, is also vulnerable to errors [Sch93]. Walls and barriers can complicate the demodulation process as they introduce more delays. This might not be a major problem as the tight synchronization requirement is an integrated part of UWB systems.

10.2 Modeling and Large-Scale Path-losses

The physical models used to predict pulse propagation in dielectric materials are based on two techniques; namely, electromagnetic wave theory and geometrical optics. The latter method is only applicable when the wavelength of the applied electromagnetic signal is considerably shorter than the dimension of object or medium being excited [Dan96, pp33].

One way of modeling large-scale path losses is to assume logarithmic attenuation with various types of structures between the transmitter and receiver antennas [Has93a]. It has also been stated that adding the individual attenuations results in the total dB loss [Has93a]. Furthermore, it is important to note that when assuming no dispersion takes place, a narrow band approximation is implied. This assumption is not as good for UWB because the dielectric constant decreases slowly with frequency.

Many results for the propagation through walls have been published. A good summary is given in [Has93a]. However, these results were often obtained at specific frequencies and measurements were not performed with sufficient care to remove the effects of scattering from edges. The measurements carried out in our lab have been crosschecked by using both time-domain and frequency-domain techniques

11 UWB Partition Dependent Propagation Modeling

Many of the narrowband channel characterization efforts are performed at specific frequencies. For UWB characterization, one has to define the pulse shape or its spectrum occupancy. Results generated for a specific pulse might not be generalized to other UWB signals.

In this section, the results for the loss of the tested materials are used to develop partition-dependent propagation models. The partition based penetration loss is defined as the path-loss difference between two locations on the opposite sides of a wall [And02]. The penetration loss is equal to the insertion loss presented earlier. The free space path-loss exponent is assumed to be n=2. The total loss along a path is the sum of free-space path loss and loss associated with partitions present along the propagation path.

In the narrowband context, the path loss with respect to1 m free space at a point located a distance d from the reference point is described by the following equation

$$PL(d) = 20\log_{10}(d) + a \times X_a + b \times X_b \ldots\ldots, \tag{50}$$

where a, b, etc., are the numbers of each partition type and X_a, X_b, etc., are their respective attenuation values measured in dB [Dur98]. To extend this concept to UWB communication channels, we introduce the frequency dependent version of equation (50),

$$PL(d, f) = 20\log_{10}(d) + a \times X_a(f) + b \times X_b(f) \ldots\ldots, \tag{51}$$

where $X_a(f)$, $X_b(f)$ are the frequency dependent insertion losses of partitions. Equation (51) gives the path loss at single frequency points. In order to find the pulse shape and the total power loss we need to find the time domain equivalent of (51) by means of inverse Fourier transform over the frequency range of the radiated signal. In doing so, we start with the radiated pulse $p_{rad}(t)$. In most wideband antennas such as TEM horns, this signal is proportional to the derivative of the input signal to the antenna. Then, we determine the spectrum of the received signal at the location of the receive antenna using the following relation ship,

$$P_{rec}(f) = \frac{P_r(f)}{\left[10^{(a \times X_a(f) + b \times X_b(f) \ldots\ldots)/20}\right] \cdot d} \tag{52}$$

It is important to note that the attenuation is applied to the radiated signal rather than the input to the antenna. The transmit antenna alters the spectrum of the input signal as illustrated in Figure 7. Starting with a Gaussian pulse, the time-domain received signal $p_{rec}(t)$ is obtained by inverse

Fourier transforming $P_{rec}(f)$. With the received pulse determined, one is able to assess pulse distortion and the total power loss. It has been assumed that the dielectric constant of the partitions remain constant over the spectrum of the radiated signal.

Example:

In this example we illustrate how to utilize the material characterization results and apply them to a partition problem. The objective is to find the power loss through a propagation path and to estimate the pulse shape and the frequency distribution of the received signal. Consider a line-of-site path with two partitions between two TEM horn antennas as shown in Figure 8a . The first partition is a sheet of glass and the second is a wooden door with the same thickness as those that have been characterized. The input signal to the antenna and that radiated from it are displayed in this figure. These signals are obtained through measurements.

To estimate the signal passed through the glass partition, Fourier transform is used to determine the spectrum of the radiated signal and the frequency dependent loss is applied to this spectrum. Inverse Fourier transform is then used to obtain the time-domain signal passed the glass sheet. The same procedure is repeated to estimate the signal passed through the wooden door partition. Examining The loss in the signal power is evident in Figure 8b. It is also noted that higher frequencies are smoothed out. The change in frequency distributions is more evident in Figure 8c. At lower frequencies, the spectra of the radiated signal, signal after the glass and signal after the wooden door are very close, whereas at higher frequencies the differences are more pronounced. This analysis is helpful in link-budget analysis and understanding of potential interference effects from indoor to outdoor environments.

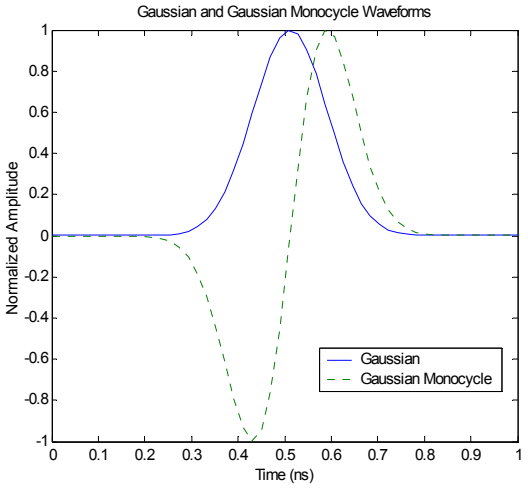

(a) Gaussian andGaussian monocycle waveforms

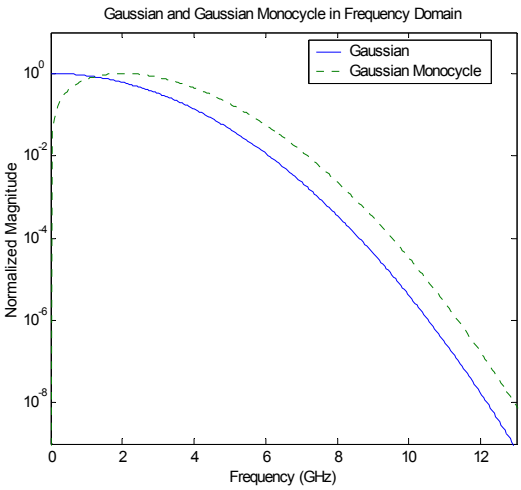

(b) Normalized spectra for Gaussian and Gaussian monocycle waveforms

Figure 7. Gaussian (TEM horn input signal) and Gaussian monocycle (TEM horn radiated signal) waveforms and their corresponding normalized spectra.

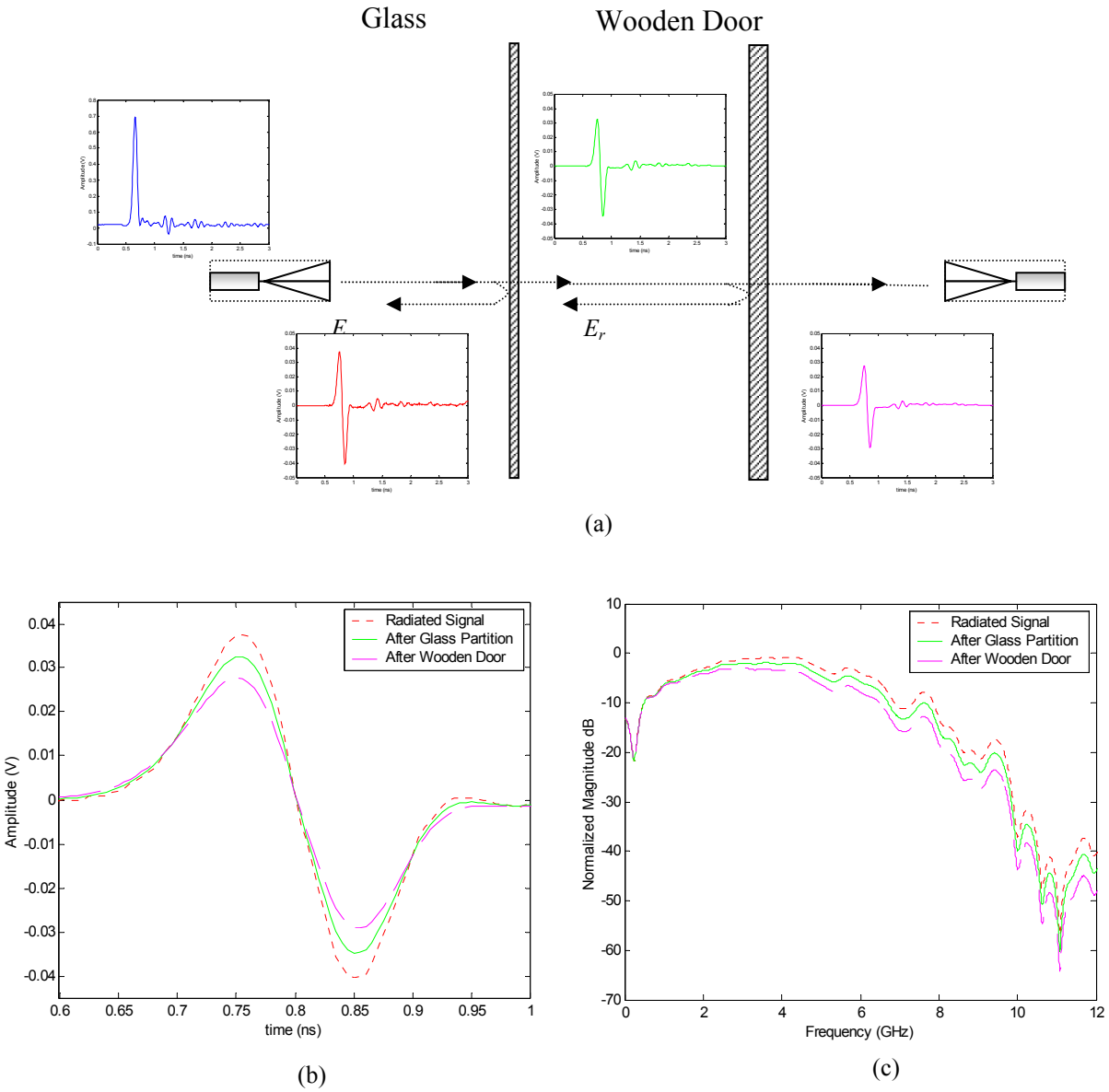

Figure 8. Illustrative example for UWB partition dependent Modeling

(a) Illustration of the partitions setup
(b) Frequency distribution of the signal at different points
(c) Radiated signal, signal after the glass partition, and the signal after the wooden door

12 Concluding Remarks

Electromagnetic characterization of materials and walls commonly encountered in indoor environments was undertaken with the aim of assessing their impacts on UWB propagation. Measurements were carried out in both time domain and frequency domain. Also, whenever possible, both single-pass and multiple-pass analysis techniques were used. A new formulation for the characterization of low-loss materials has been presented which requires solving real equations only and converges more rapidly, thus requires much less computation time than that based on solving the complex equation relating the insertion transfer function to the dielectric constant of the material under test. The new formulation can be used to accurately characterize many materials of practical applications which are low loss. Results from different techniques agree well, thus ensuring the reliability and accuracy of the measurements. Ten different materials were tested and results were presented in terms of insertion loss and dielectric constant. The presented results should serve as a basis for further studies in developing appropriate models for UWB channels. The results are also useful in UWB link budget analysis.

APPENDICES

Appendix A

A1. Multi-Pass, Complex Dielectric Constant Equation

The derivation of the complex dielectric constant equation based on a multi-pass analysis is presented in this appendix. Assuming a uniform plane-wave normally incident on an infinite material slab, the partial reflection coefficient at the first boundary, denoted as ρ, is given by

$$\rho = \frac{\eta_2 - \eta_1}{\eta_2 + \eta_1} \tag{A 1-1}$$

where η_1 and η_2 are the intrinsic impedances of air (essentially free space) and the material of the slab under test, respectively. The transmission coefficient at the first boundary is obtained from the relationship $\tau_1 = 1 + \rho$. At the second boundary, when propagation is in the direction of the material toward air, the partial reflection coefficient is equal to $-\rho$, while the partial transmission coefficient is $\tau_2 = 1 - \rho$. Thus, the first partial transmitted wave through the slab is $T\tau_1\tau_2 = T(1-\rho^2)\mathbf{E}_i$, where $\mathbf{E}_i$ is the incident field and

$$T = e^{-\gamma d} \tag{A 1-2}$$

accounts for propagation through the slab thickness, with γ being the complex propagation constant of the slab. Using the bounce diagram shown in Figure A1-1, the overall transmission coefficient through the slab, which is the same as the scattering parameter S_{21}, is obtained from

$$S_{21} = T\left(1-\rho^2\right)\left(1+\rho^2T^2+\rho^4T^4+\cdots\right) = \frac{T\left(1-\rho^2\right)}{1-\rho^2T^2} \tag{A 1-3}$$

In case of the free-space measurements $\rho_{free-space} = 0$, and S_{21} is given by

$$S_{21air} = T_a = e^{j\beta_a d} \tag{A 1-4}$$

Relating the two measurements, one can write the insertion transfer function as

$$H(j\omega) = \frac{S_{21}}{S_{21air}} = \frac{T(1-\rho^2)}{T_a(1-\rho^2 T^2)} \qquad \text{(A 1-5)}$$

By substituting (A2-1) and (A2-2) into (A2-5) one can write

$$\left(x + \frac{1}{x}\right)\sinh(xP) + 2\cosh(xP) - \frac{2}{S_{21}} = 0 \qquad \text{(A 1-6)}$$

where $x = \sqrt{\varepsilon_r}$ and $P = j2\pi f \frac{d}{c}$, which is the equation used for multi-pass complex search.

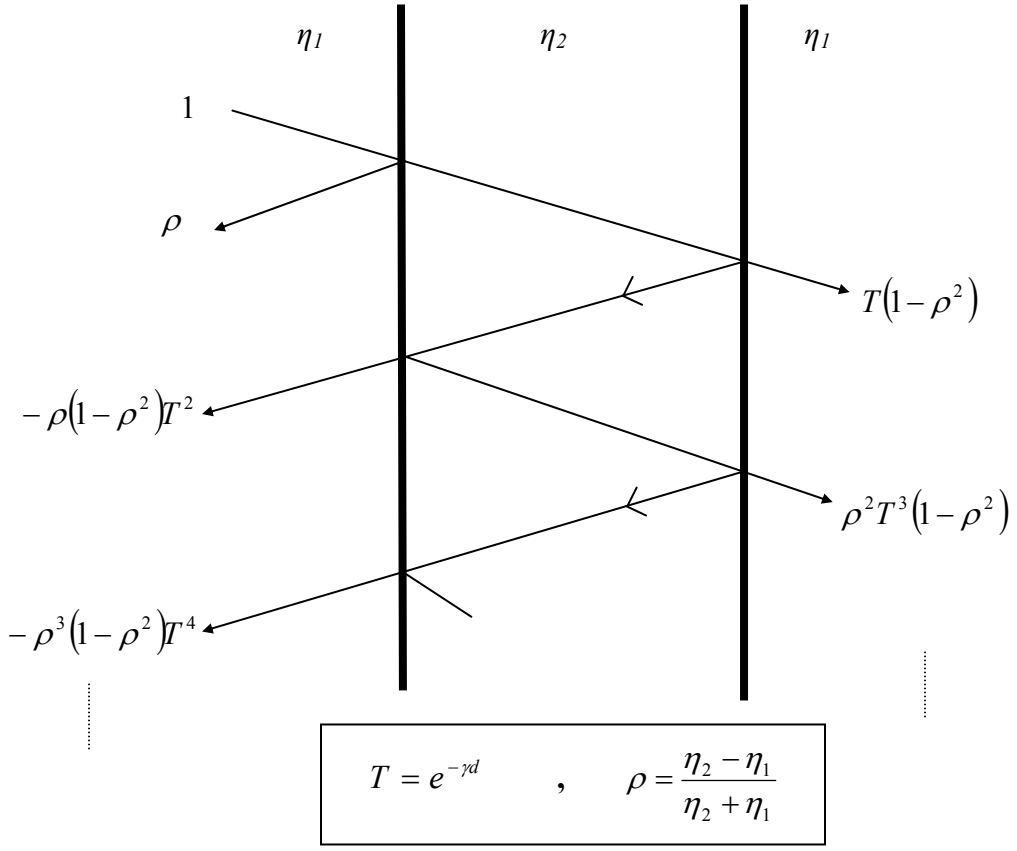

Figure A2-1: Bounce Diagram for propagation through a slab

A2. Proof of Equation (42) being Valid with Negative Sign

Here, it is proved that the solution for X with a negative sign in front of the square root is the only valid solution. Whenever a solution exists, we must have

$$\left[\cos(2\beta d)(\varepsilon_r'-1)^2+\frac{8\varepsilon_r'}{|H(j\omega)|^2}\right]^2-(\varepsilon_r'-1)^4>0 \qquad \text{(A 2-1)}$$

(A2-1) is rewritten as

$$\left[\cos(2\beta d)(\varepsilon_r'-1)^2+\frac{8\varepsilon_r'}{|H(j\omega)|^2}-(\varepsilon_r'-1)^2\right]\cdot\left[\cos(2\beta d)(\varepsilon_r'-1)^2+\frac{8\varepsilon_r'}{|H(j\omega)|^2}+(\varepsilon_r'-1)^2\right]>0 \qquad \text{(A 2-2)}$$

The second square bracket in (A2-2) is always positive, because

$$\left[\cos(2\beta d)(\varepsilon_r'-1)^2+\frac{8\varepsilon_r'}{|H(j\omega)|^2}+(\varepsilon_r'-1)^2\right]=\left[(\varepsilon_r'-1)^2(1+\cos(2\beta d))+\frac{8\varepsilon_r'}{|H(j\omega)|^2}\right]>0, \qquad \text{(A 2-3)}$$

Thus, the first square bracket should be positive too. That is,

$(\varepsilon_r'-1)^2>0$, $(1+\cos(2\beta d))>0$, and $\dfrac{8\varepsilon_r'}{|H(j\omega)|^2}>0$.

Thus,

$$\cos(2\beta d)(\varepsilon_r'-1)^2+\frac{8\varepsilon_r'}{|H(j\omega)|^2}-(\varepsilon_r'-1)^2>0$$

or

$$\cos(2\beta d)(\varepsilon_r'-1)^2+\frac{8\varepsilon_r'}{|H(j\omega)|^2}>(\varepsilon_r'-1)^2>0 \qquad \text{(A 2-4)}$$

Hence, the solution for X with a negative sign in front of the square root is always >0, i.e.,

$$X = \frac{\left[\cos(2\beta d)(\varepsilon_r' - 1)^2 + 8\frac{\varepsilon_r'}{|H(j\omega)|^2}\right] - \sqrt{\left[\cos(2\beta d)(\varepsilon_r' - 1)^2 + 8\frac{\varepsilon_r'}{|H(j\omega)|^2}\right]^2 - (\varepsilon_r' - 1)^4}}{\left(\sqrt{\varepsilon_r'} - 1\right)^4} > 0 \tag{A 2-5}$$

On the other hand, X should be less than 1 (otherwise instead of attenuation we have amplification). Now, we show that the solution for X with positive sign in front of the square root is greater than 1 and thus not acceptable

$$\frac{\left[\cos(2\beta d)(\varepsilon_r' - 1)^2 + 8\frac{\varepsilon_r'}{|H(j\omega)|^2}\right] + \sqrt{\left[\cos(2\beta d)(\varepsilon_r' - 1)^2 + 8\frac{\varepsilon_r'}{|H(j\omega)|^2}\right]^2 - (\varepsilon_r' - 1)^4}}{\left(\sqrt{\varepsilon_r'} - 1\right)^4} \stackrel{?}{>} 1 \tag{A 2-6}$$

Using the condition in (A2-4) in (A2-6), we have

$$\frac{(\varepsilon_r' - 1)^2 + \sqrt{\left[\cos(2\beta d)(\varepsilon_r' - 1)^2 + 8\frac{\varepsilon_r'}{|H(j\omega)|^2}\right]^2 - (\varepsilon_r' - 1)^4}}{\left(\sqrt{\varepsilon_r'} - 1\right)^4} \stackrel{?}{>} 1 \tag{A 2-7}$$

or

$$\frac{(\varepsilon_r' - 1)^2}{\left(\sqrt{\varepsilon_r'} - 1\right)^4} + \frac{\sqrt{\left[\cos(2\beta d)(\varepsilon_r' - 1)^2 + 8\frac{\varepsilon_r'}{|H(j\omega)|^2}\right]^2 - (\varepsilon_r' - 1)^4}}{\left(\sqrt{\varepsilon_r'} - 1\right)^4} \stackrel{?}{>} 1 \tag{A 2-8}$$

The second term is positive so it sufficient to prove that

$$\left(\frac{\varepsilon_r' - 1}{\left(\sqrt{\varepsilon_r'} - 1\right)^2}\right)^2 \stackrel{?}{>} 1 \tag{A 2-9}$$

Or

$$\frac{\varepsilon_r' - 1}{\left(\sqrt{\varepsilon_r'} - 1\right)^2} \stackrel{?}{>} 1 \tag{A 2-10}$$

which leads to $\varepsilon_r' - 1 \stackrel{?}{>} \varepsilon_r' + 1 - 2\sqrt{\varepsilon_r'}$ or $\varepsilon_r' \stackrel{?}{>} 1$ which is obviously true. Consequently, the solution of X with "+" sign in front of the square root is not valid. The correct solution is the one with the "-" sign in front of the square root.

Appendix B

B1. Through-the-Wall Signal Processing Plots and Material Parameters for Sample Door

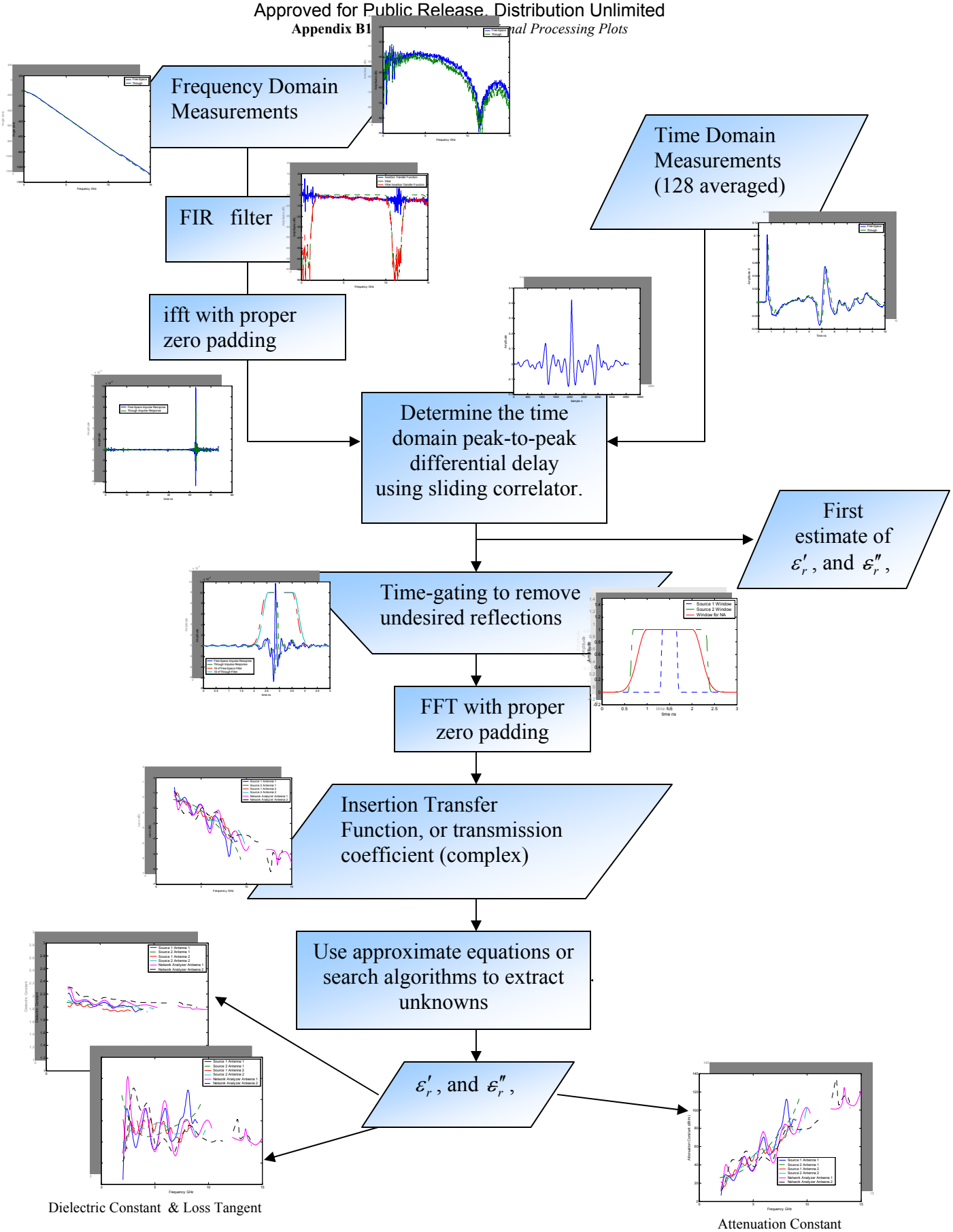

Figure B1-1. Through the wall and material characterization procedure flowchart

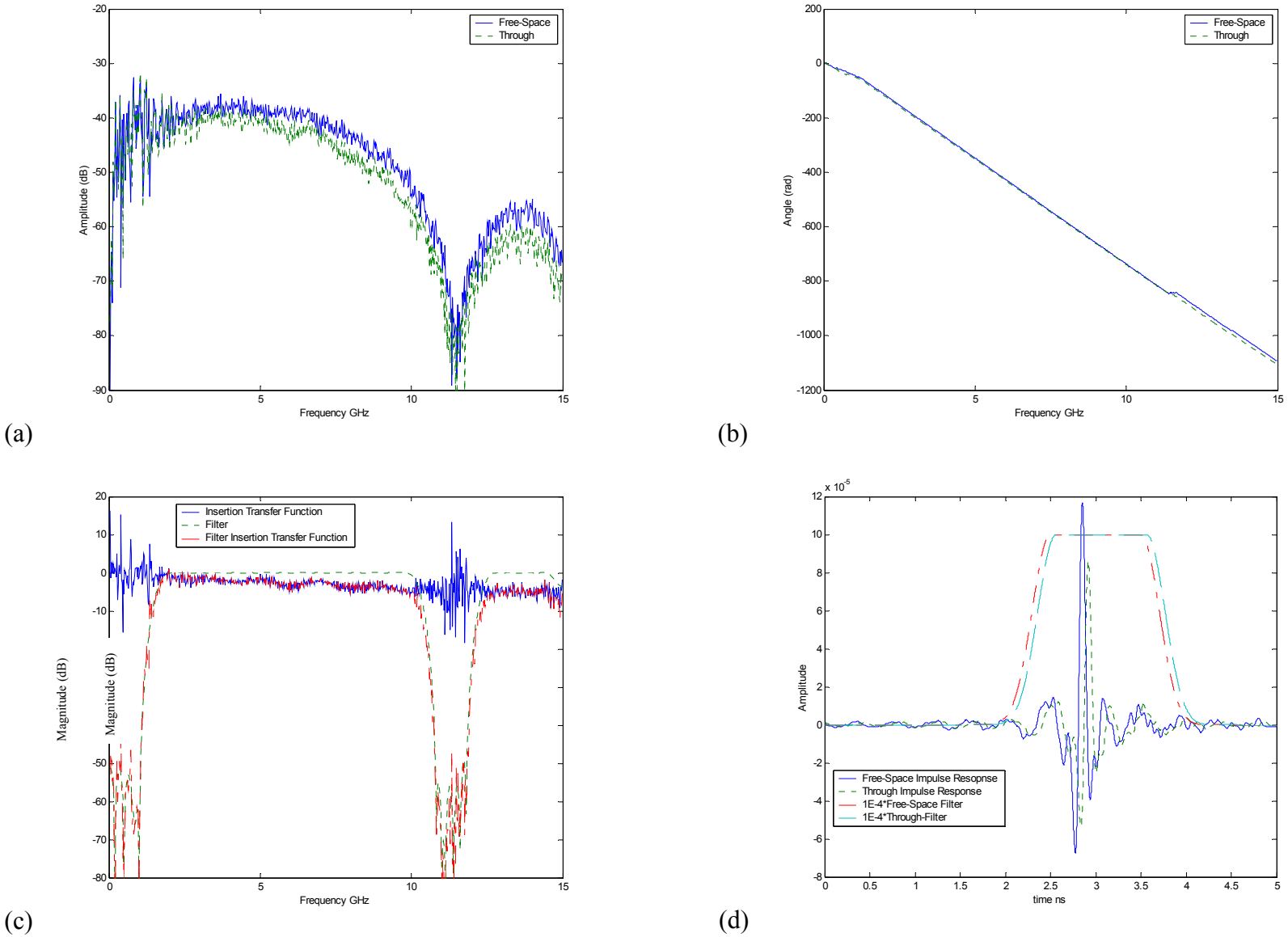

Figure B1-2. Illustration of the frequency domain measurements, (a) Measured Magnitude, (b) Measured phase, (c) Filter and filtered un-gated insertion transfer function, and (d) Impulse response and weighted gating window

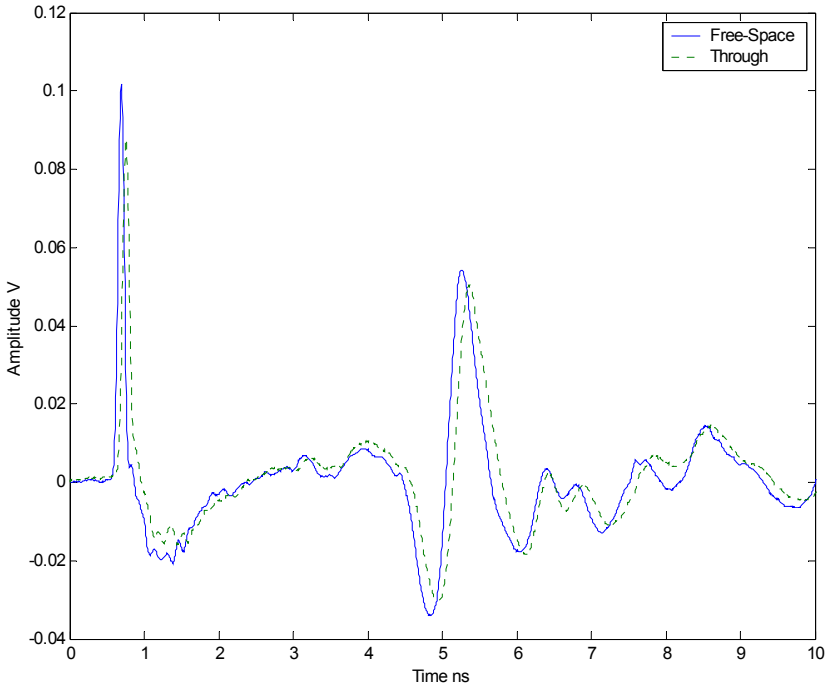

(a)

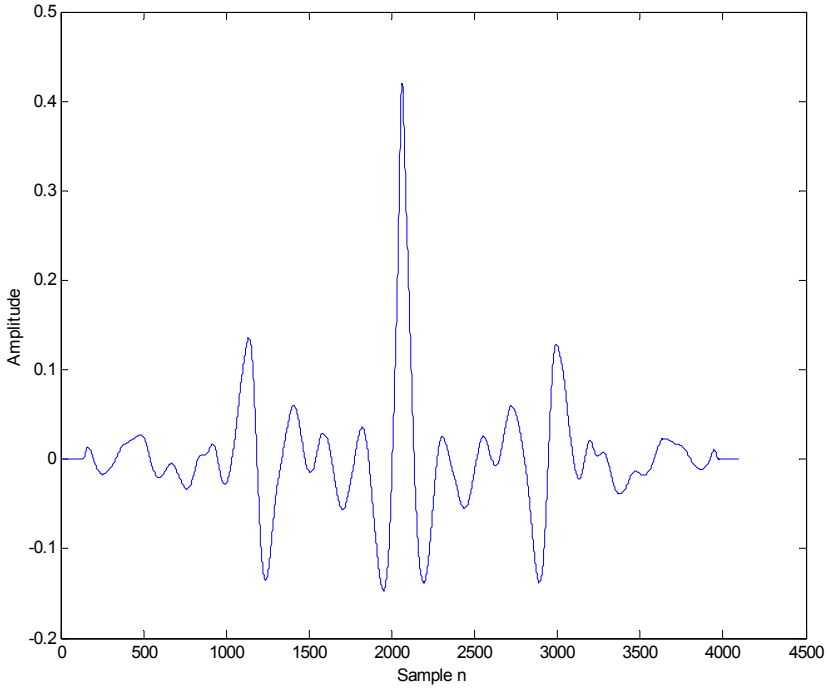

(b)

Figure B1-3. Illustration of the Time domain measurements,
(a) Measured 'through' and 'free space' signals
(b) Illustration of the correlation function to estimate the time delay.

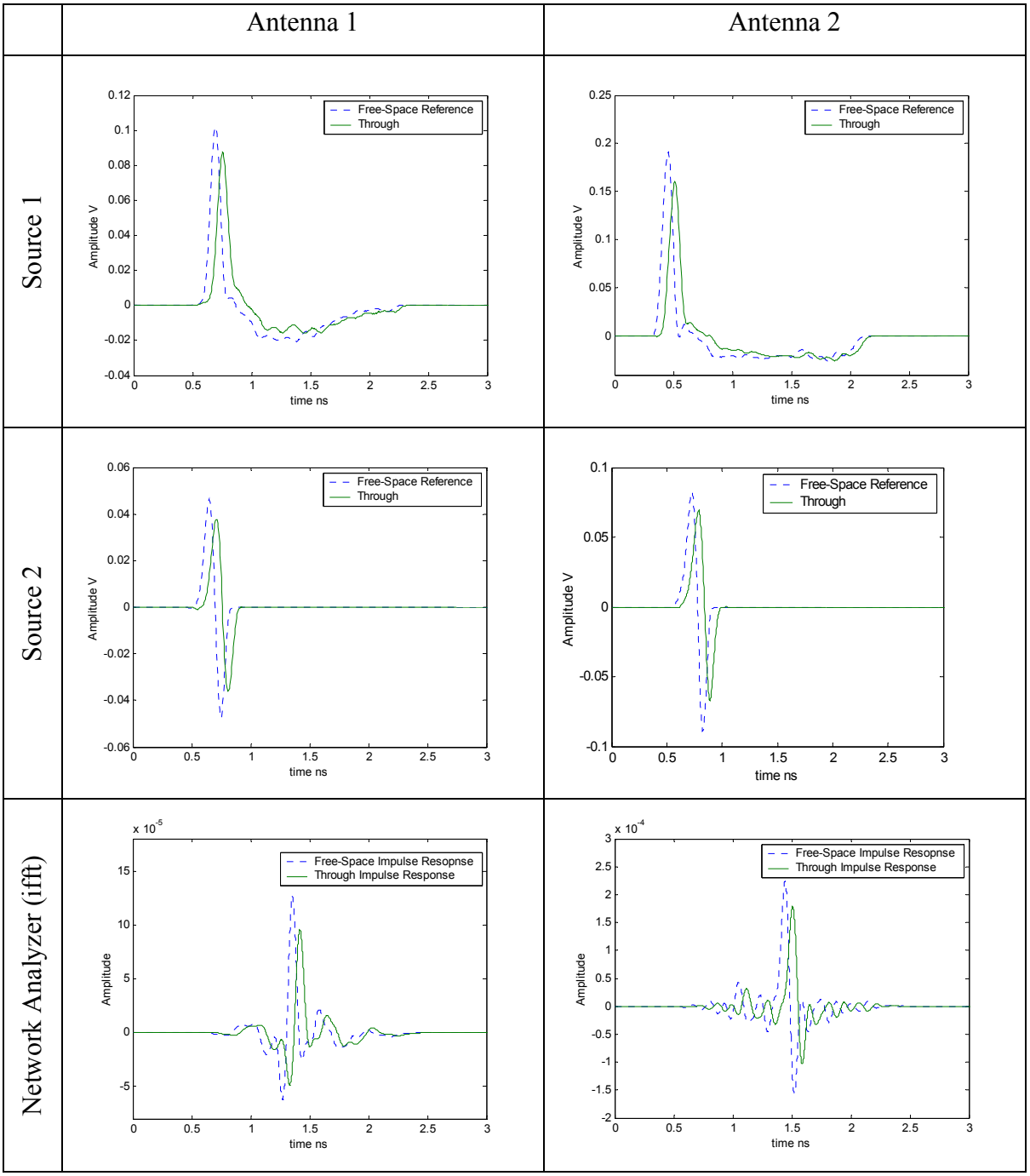

Figure B1-4. Time domain representation of the six different measurements for the sample door

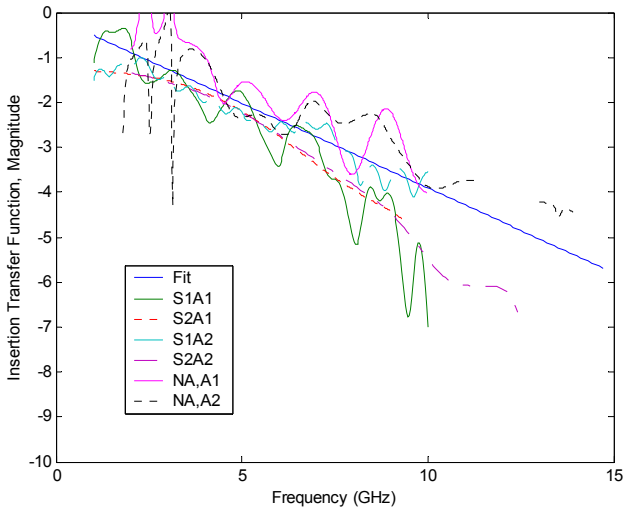

(a)

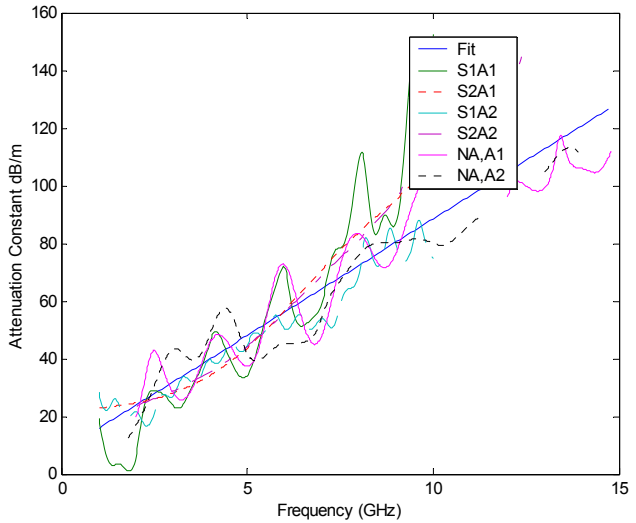

(b)

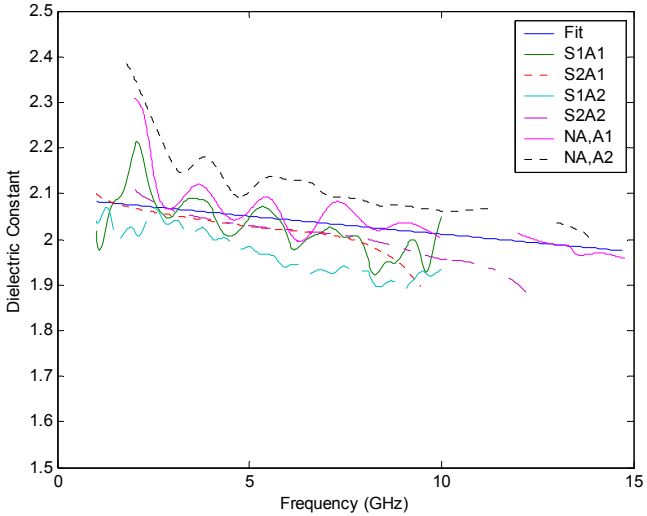

(c)

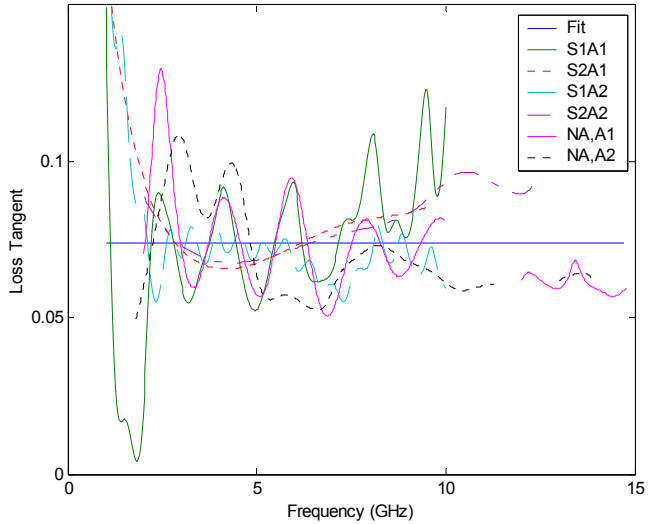

(d)

Figure B1-5. Comparison for the sample door parameters extracted using different measurement techniques, (a) insertion transfer function , magnitude, (b) attenuation constant, (c) dielectric constant, and (d) loss tangent.

B2. Through-the-Wall and Material Characterization Plots

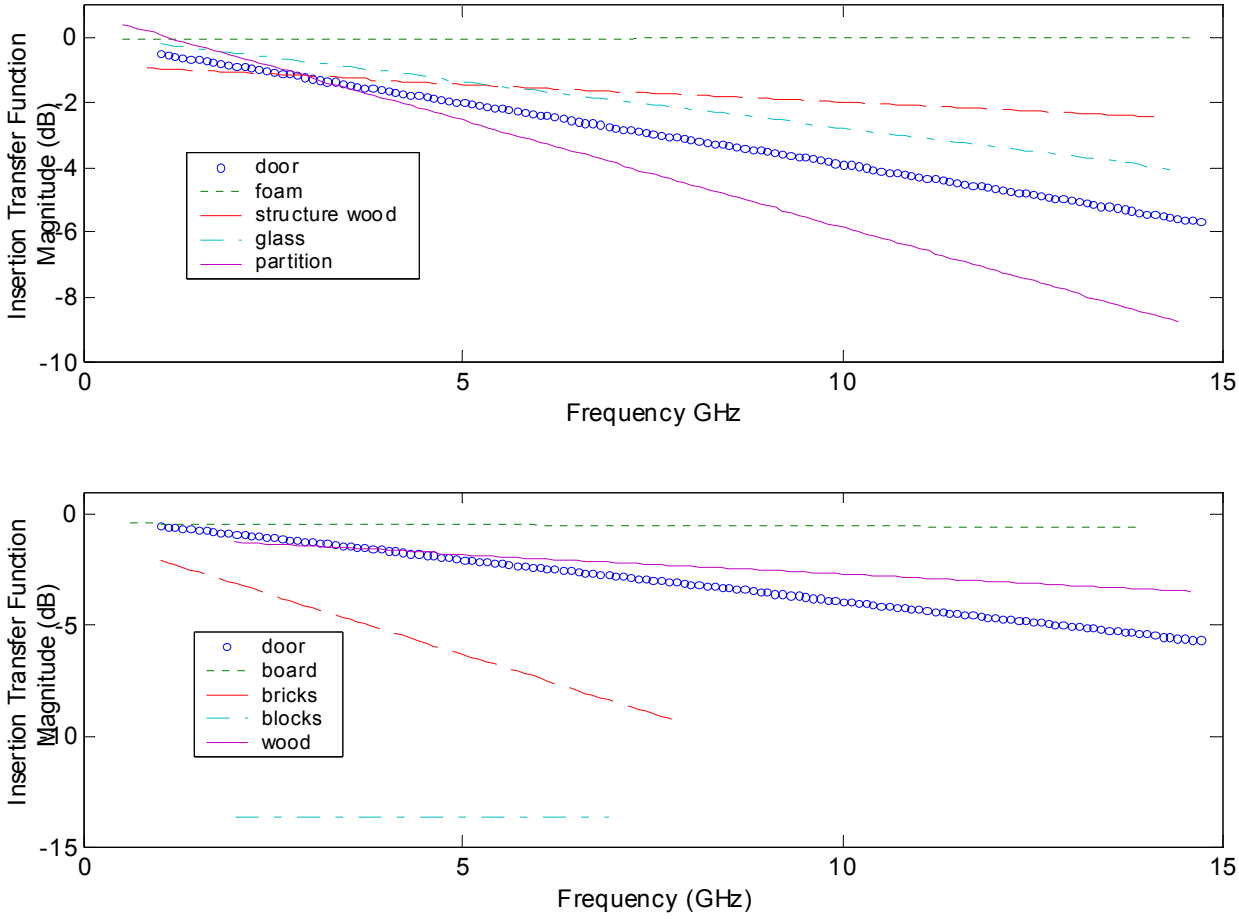

Figure B2-1. Insertion Transfer Function plotted versus frequency for different materials used.

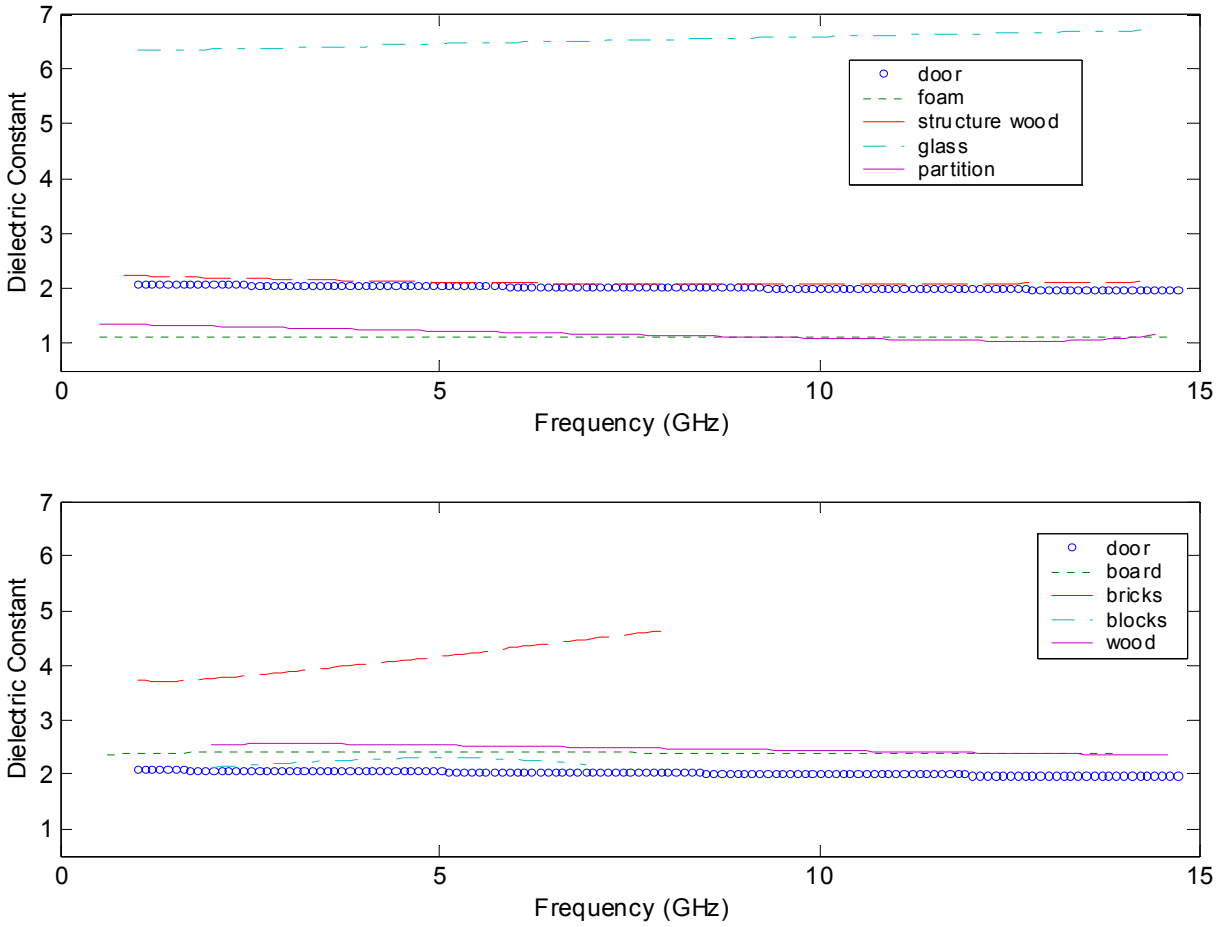

Figure B2- 10. Dielectric constant plotted versus frequency for different materials used.

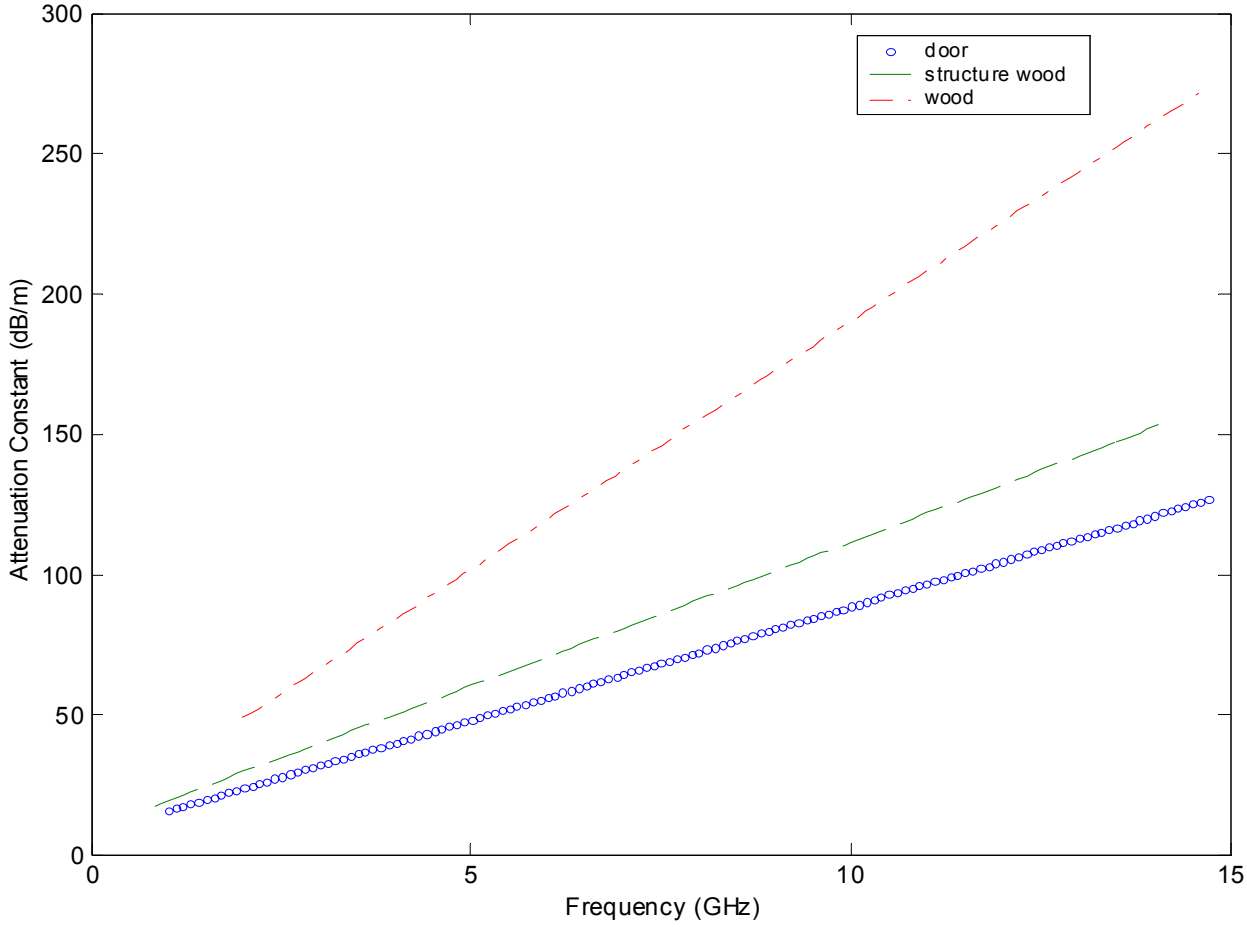

Figure B2-11. Attenuation constant plotted versus frequency for different materials used.

Blocks wall

Board

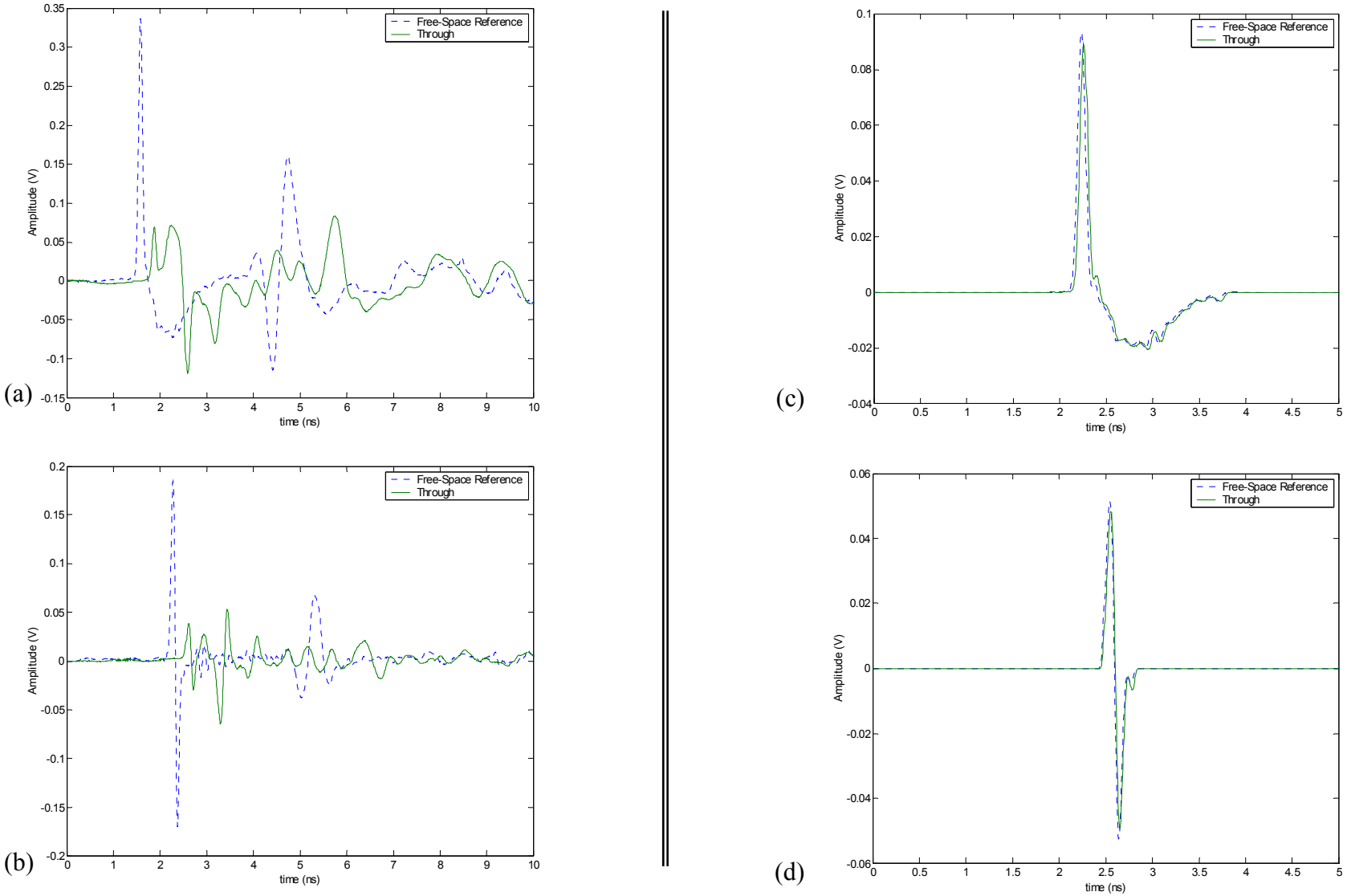

Figure B2-12. Blocks wall and Wallboard 'free-space' and 'through' measurements. Plots (a) and (b) are ungated time-domain waveforms for blocks as the material using sources #1 and #2, respectively. Plots (c) and (d) are time-gated waveforms for the board using sources #1 and #2, respectively.

Cloth Partition

Structure Wood

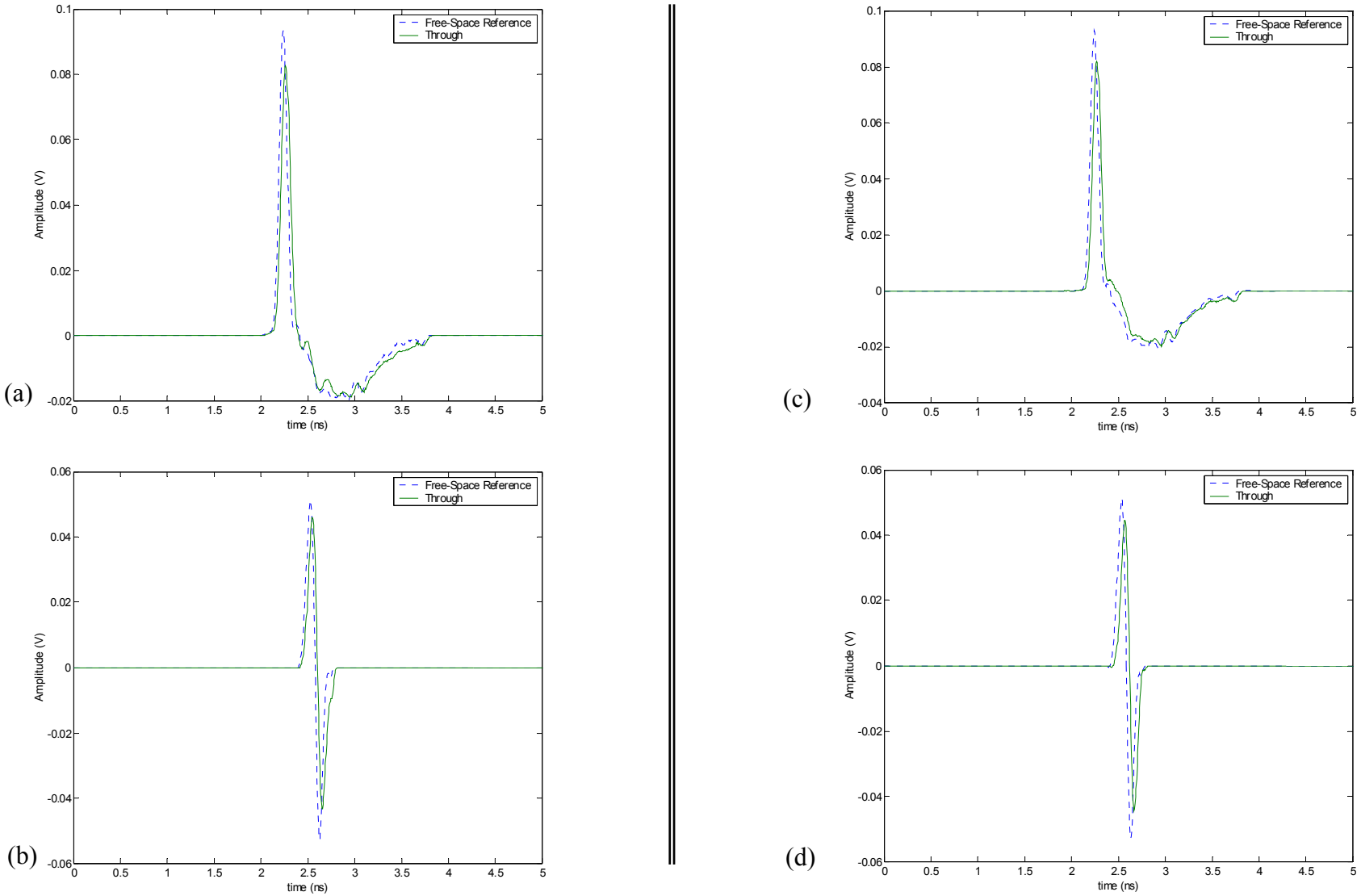

Figure B2-13. Cloth office partition and structure wood 'free-space' and 'through' measurements. Plots (a) and (b) are time-gated waveforms for cloth partition as the material using sources #1 and #2, respectively. Plots (c) and (d) are time-gated waveforms for the structure wood using sources #1 and #2, respectively.

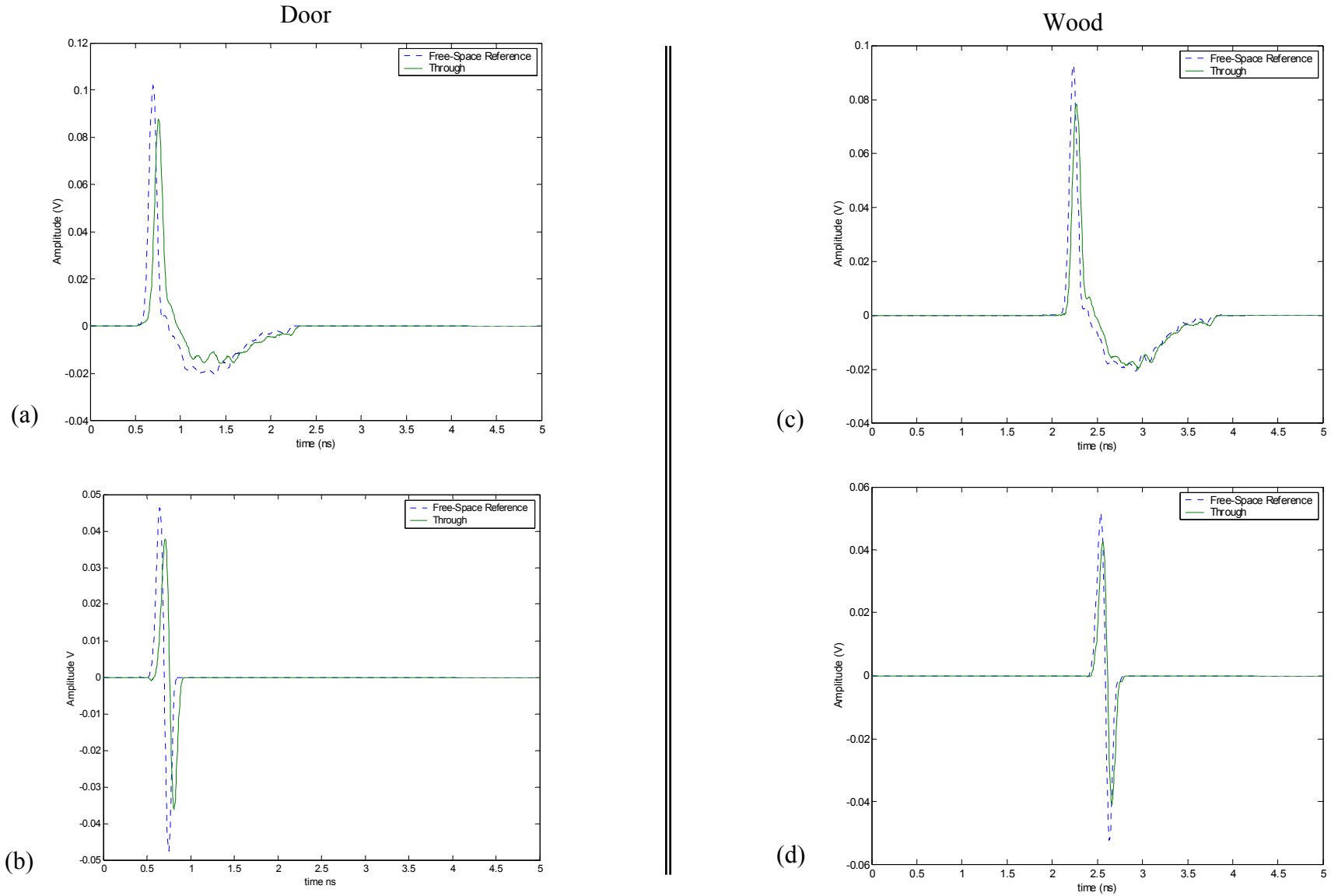

Figure B2-14. Door and wood 'free-space' and 'through' measurements. Plots (a) and (b) are time-gated waveforms for sample door as the material using sources #1 and #2, respectively. Plots (c) and (d) are time-gated waveforms for the wood using sources #1 and #2, respectively.

Glass

Styrofoam

(a)

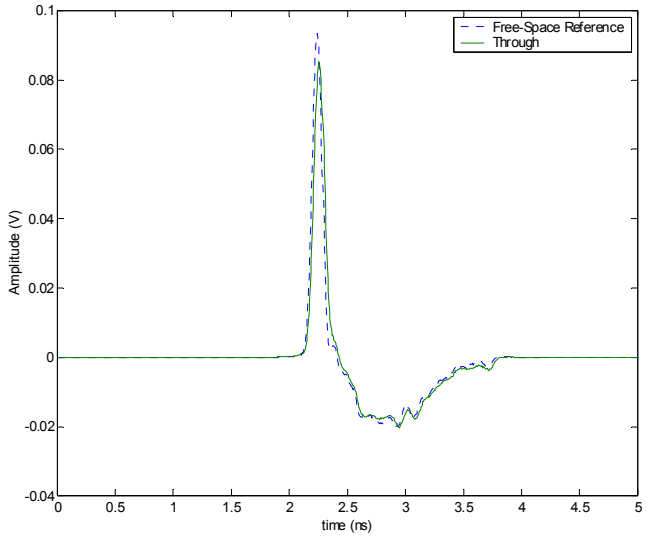

(b)

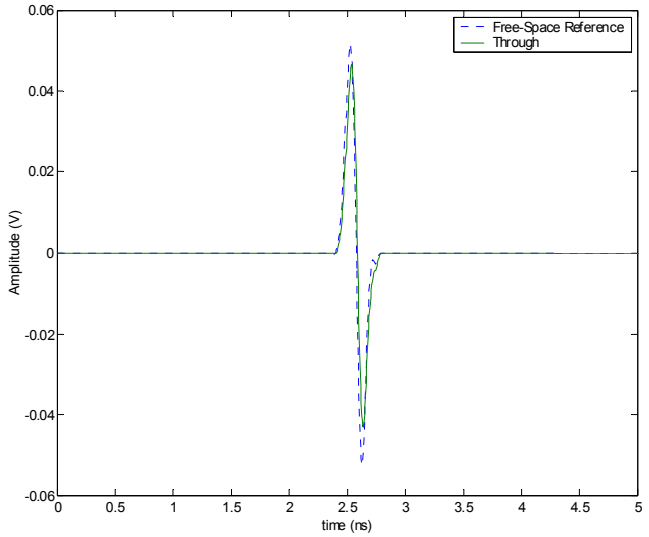

(c)

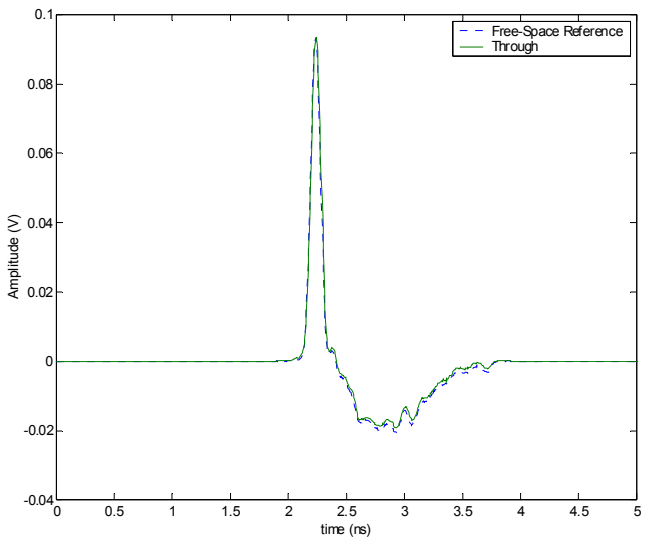

(d)

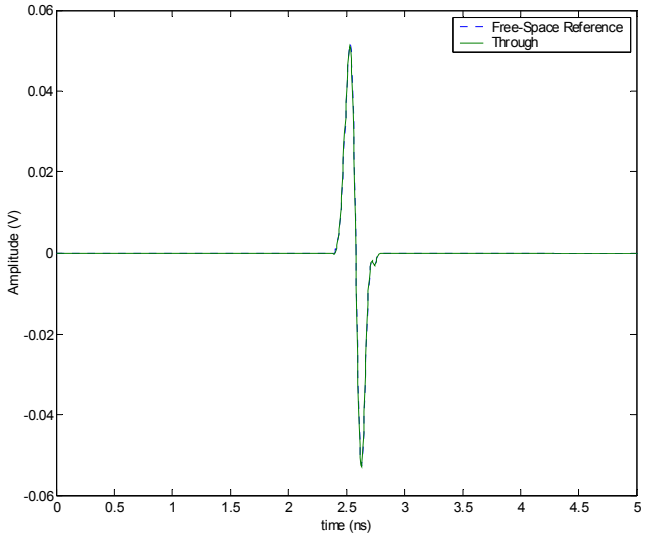

Figure B2-15. Glass and Styrofoam 'free-space' and 'through' measurements. Plots (a) and (b) are time-gated waveforms for glass as the material using sources #1 and #2, respectively. Plots (c) and (d) are time-gated waveforms for Styrofoam using sources #1 and #2, respectively.

Bricks wall

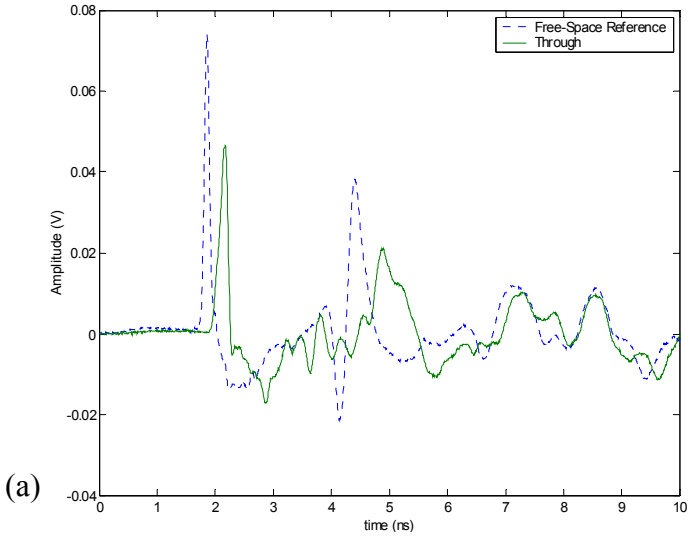

(a)

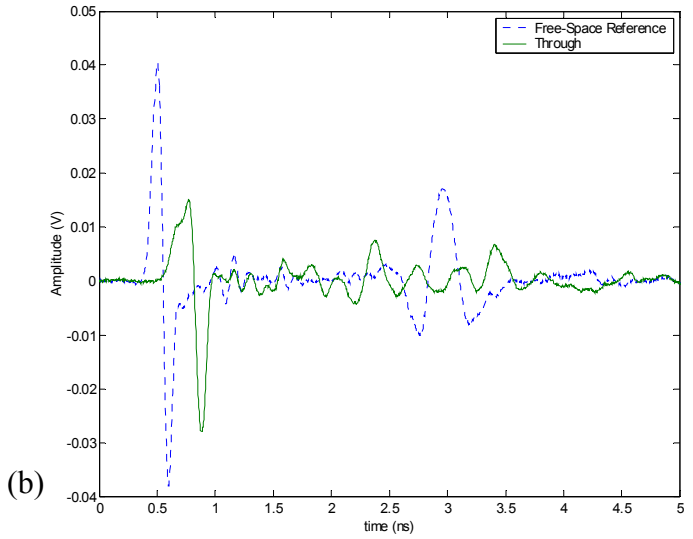

(b)

Reinforced Concrete Pillars (c) Whittemore and (d)TDL)

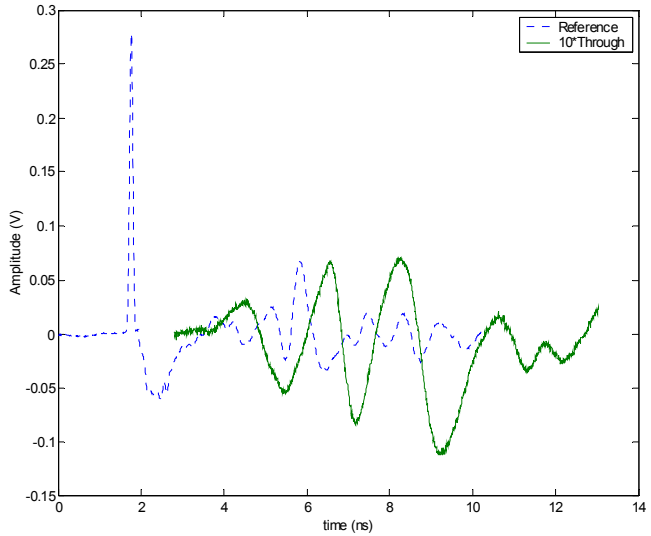

(c)

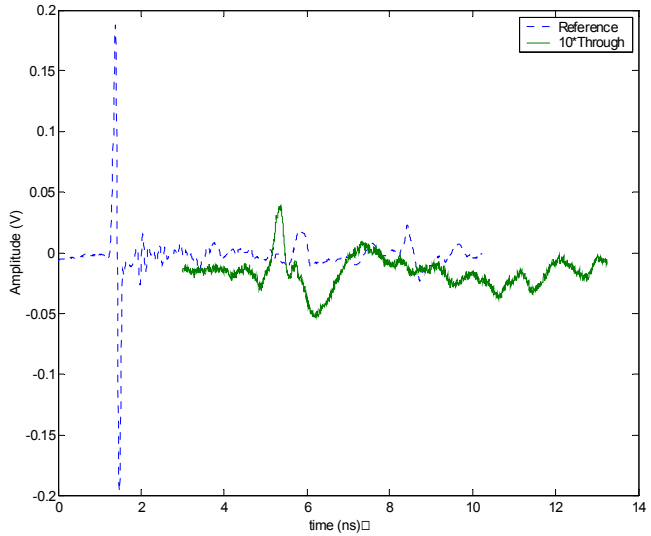

(d)

Figure B2-16. Bricks wall and Reinforced concrete pillars 'free-space' and 'through' measurements. Plots (a) and (b) are ungated time-domain waveforms for bricks as the material using sources #1 and #2, respectively. Plots (c) and (d) are ungated waveforms for reinforced concrete pillars (Whittemore and TDL) using sources #1 and #2, respectively.

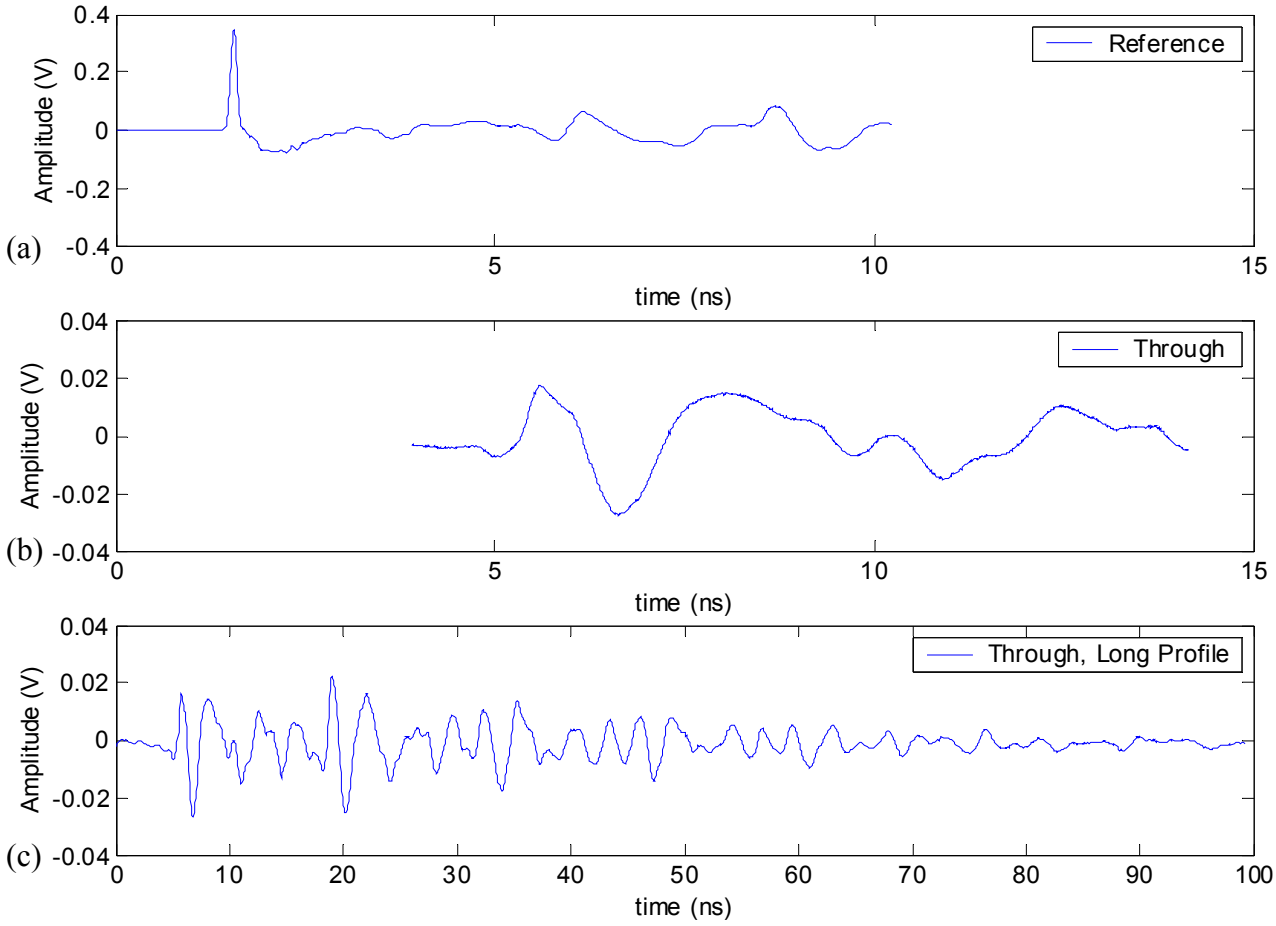

Figure B2-17. TDL Reinforced concrete pillar 'free-space' and 'through' measurements. Plot (a) is the reference measurement. Plot (b) indicates the measurement through the reinforced concrete pillar (TDL). Plot (c) demonstrates a longer profile for the through measurement.

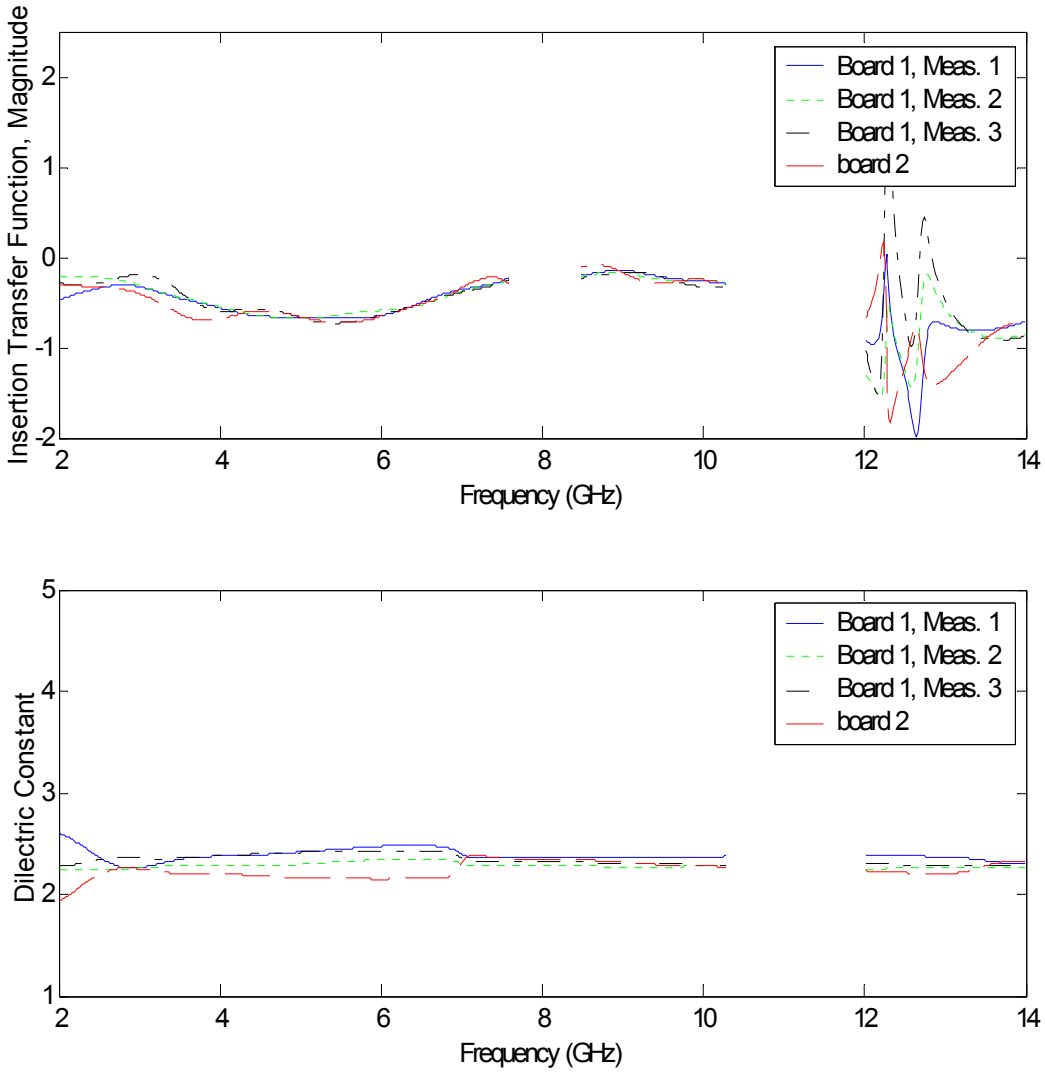

Figure B2-18. Repeatability and variability of frequency domain measurements

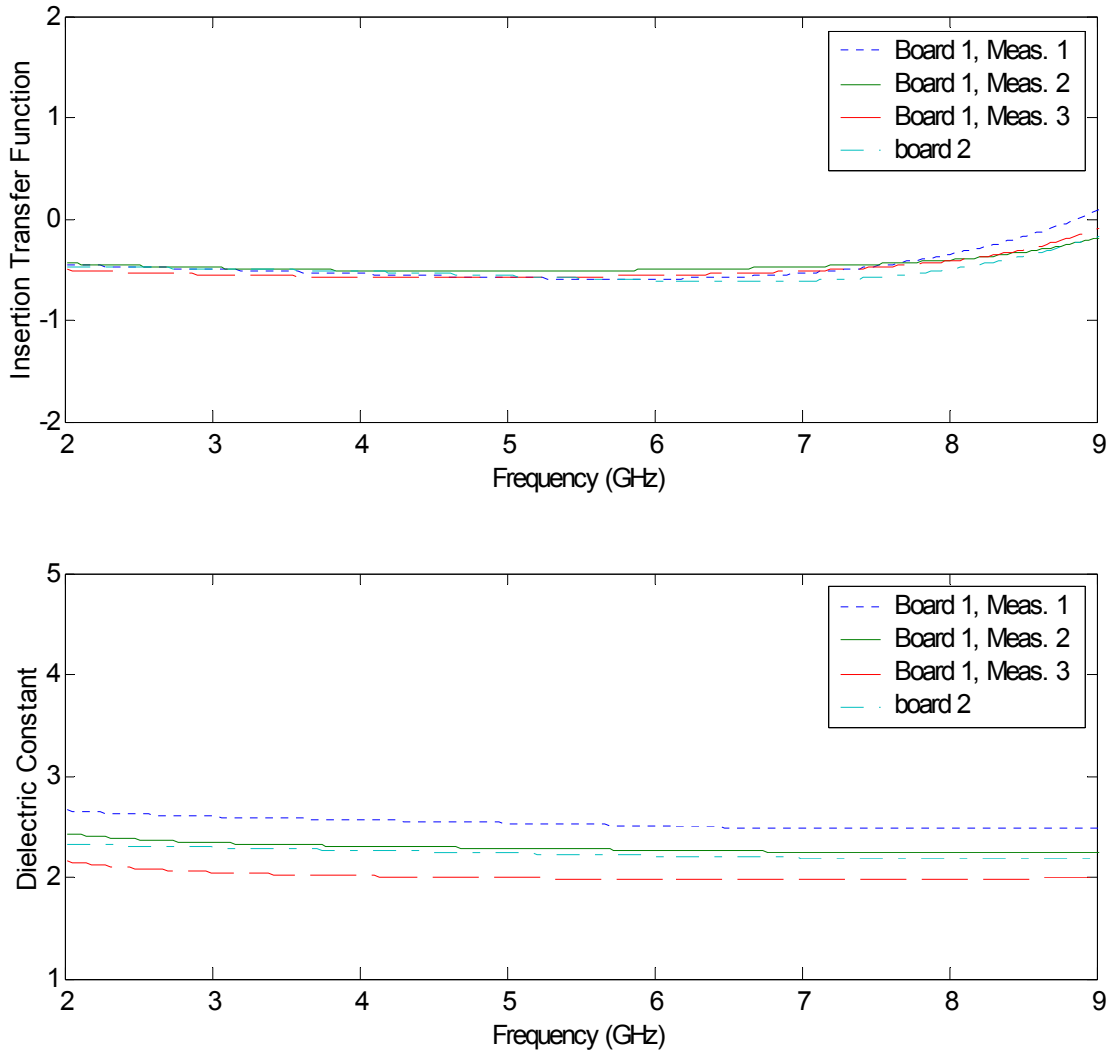

Figure B2-19. Repeatability and variability of time domain measurements

B3. Tables of Measurements

Note 1: For some materials accurate measurements in the lower and higher portions of the frequency range of operation could not be made because of very low received power due to significant drop in the antenna gain and high attenuation of the material under test.

Note 2: For homogenous material slabs such as structure wood, sample door, and ply wood, in addition to loss, attenuation coefficients measured in dB/m are also provided.

Table B3- 1 Measured Data for Wallboard

Material	**Width** ***(cm)***	**Length** ***(cm)***	**Thickness** ***(cm)***
Wallboard	121.8	196.9	1.16992

Frequency (GHz)	**Loss (dB)**	**Dielectric Constant**
0.62	**0.40**	**2.37**
1.32	**0.41**	**2.40**
2.02	**0.42**	**2.41**
2.72	**0.43**	**2.41**
3.42	**0.44**	**2.42**
4.12	**0.45**	**2.41**
4.82	**0.46**	**2.41**
5.52	**0.47**	**2.41**
6.22	**0.48**	**2.41**
6.92	**0.49**	**2.41**
7.62	**0.49**	**2.40**
8.32	**0.50**	**2.40**
9.02	**0.51**	**2.40**
9.72	**0.52**	**2.40**
10.42	**0.53**	**2.39**
11.12	**0.54**	**2.39**
11.82	**0.55**	**2.39**
12.52	**0.56**	**2.38**
13.22	**0.57**	**2.38**
13.92	**0.58**	**2.38**

Table B3- 2 Measured Data for Cloth Partition

Material	**Width** ***(cm)***	**Height** ***(cm)***	**Thickness** ***(cm)***
Cloth Partition	140.7	153.1	5.9309

Frequency (GHz)	**Loss (dB)**	**Dielectric Constant**
0.52	**0.00**	**1.36**
1.22	**0.06**	**1.34**
1.92	**0.53**	**1.32**
2.62	**0.99**	**1.29**
3.32	**1.45**	**1.27**
4.02	**1.91**	**1.25**
4.72	**2.37**	**1.23**
5.42	**2.84**	**1.21**
6.12	**3.30**	**1.19**
6.82	**3.76**	**1.17**
7.52	**4.22**	**1.15**
8.22	**4.68**	**1.14**
8.92	**5.15**	**1.12**
9.62	**5.61**	**1.10**
10.32	**6.07**	**1.08**
11.02	**6.53**	**1.07**
11.72	**6.99**	**1.05**
12.42	**7.46**	**1.04**
13.12	**7.92**	**1.04**
13.82	**8.38**	**1.07**

Table B3- 3 Measured Data for Structure Wood

Material	Width *(cm)*	Length *(cm)*	Thickness *(cm)*
Structure Wood	121.5	197.8	2.06781

Frequency (GHz)	Loss (dB)	Dielectric Constant	Attenuation (dB/m)
0.81	**0.96**	**2.24**	**17.41**
1.51	**1.04**	**2.22**	**24.57**
2.21	**1.12**	**2.20**	**31.74**
2.91	**1.19**	**2.17**	**38.90**
3.61	**1.27**	**2.15**	**46.06**
4.31	**1.35**	**2.14**	**53.22**
5.01	**1.43**	**2.12**	**60.38**
5.71	**1.51**	**2.11**	**67.54**
6.41	**1.59**	**2.10**	**74.70**
7.11	**1.67**	**2.09**	**81.87**
7.81	**1.75**	**2.08**	**89.03**
8.51	**1.83**	**2.08**	**96.19**
9.21	**1.91**	**2.08**	**103.35**
9.91	**1.99**	**2.08**	**110.51**
10.61	**2.07**	**2.08**	**117.67**
11.31	**2.15**	**2.08**	**124.83**
12.01	**2.23**	**2.09**	**132.00**
12.71	**2.30**	**2.10**	**139.16**
13.41	**2.38**	**2.11**	**146.32**
14.11	**2.46**	**2.12**	**153.48**

Table B3- 4 Measured Data for Sample Door

Material	Width *(cm)*	Height *(cm)*	Thickness *(cm)*
Sample door	90.70	211.8	4.44754

Frequency (GHz)	Loss (dB)	Dielectric Constant	Attenuation (dB/m)
1.01	**0.51**	**2.08**	**15.78**
1.71	**0.77**	**2.08**	**21.44**
2.41	**1.04**	**2.07**	**27.10**
3.11	**1.30**	**2.07**	**32.76**
3.81	**1.56**	**2.06**	**38.42**
4.51	**1.83**	**2.05**	**44.08**
5.21	**2.09**	**2.05**	**49.74**
5.91	**2.36**	**2.04**	**55.40**
6.61	**2.62**	**2.04**	**61.06**
7.31	**2.89**	**2.03**	**66.72**
8.01	**3.15**	**2.03**	**72.38**
8.71	**3.42**	**2.02**	**78.04**
9.41	**3.68**	**2.02**	**83.70**
10.11	**3.94**	**2.01**	**89.36**
10.81	**4.21**	**2.00**	**95.02**
11.51	**4.47**	**2.00**	**100.68**
12.21	**4.74**	**1.99**	**106.34**
12.91	**5.00**	**1.99**	**112.00**
13.61	**5.27**	**1.98**	**117.66**
14.31	**5.53**	**1.98**	**123.32**

Table B3- 5 Measured Data for Ply Wood

Material	Width *(cm)*	Length *(cm)*	Thickness *(cm)*
Ply Wood	121.9	197.51	1.52146

Frequency (GHz)	Loss (dB)	Dielectric Constant	Attenuation (dB/m)
2.00	**1.27**	**2.55**	**48.68**
2.70	**1.40**	**2.57**	**61.07**
3.40	**1.52**	**2.57**	**73.46**
4.10	**1.65**	**2.56**	**85.84**
4.80	**1.77**	**2.55**	**98.23**
5.50	**1.89**	**2.54**	**110.62**
6.20	**2.02**	**2.52**	**123.01**
6.90	**2.14**	**2.51**	**135.40**
7.60	**2.26**	**2.49**	**147.79**
8.30	**2.39**	**2.48**	**160.18**
9.00	**2.51**	**2.46**	**172.57**
9.70	**2.64**	**2.45**	**184.95**
10.40	**2.76**	**2.44**	**197.34**
11.10	**2.88**	**2.42**	**209.73**
11.80	**3.01**	**2.41**	**222.12**
12.50	**3.13**	**2.40**	**234.51**
13.20	**3.26**	**2.38**	**246.90**
13.90	**3.38**	**2.37**	**259.29**
14.60	**3.50**	**2.35**	**271.68**

Table B3- 6 Measured Data for Glass

Material	**Width** ***(cm)***	**Length** ***(cm)***	**Thickness** ***(cm)***
Glass	91.44	111.76	0.235661

Frequency (GHz)	**Loss (dB)**	**Dielectric Constant**
1.01	**0.19**	**6.35**
1.71	**0.39**	**6.37**
2.41	**0.60**	**6.39**
3.11	**0.80**	**6.41**
3.81	**1.00**	**6.43**
4.51	**1.21**	**6.44**
5.21	**1.41**	**6.46**
5.91	**1.61**	**6.48**
6.61	**1.81**	**6.50**
7.31	**2.02**	**6.52**
8.01	**2.22**	**6.54**
8.71	**2.42**	**6.55**
9.41	**2.62**	**6.57**
10.11	**2.83**	**6.59**
10.81	**3.03**	**6.61**
11.51	**3.23**	**6.63**
12.21	**3.43**	**6.65**
12.91	**3.64**	**6.67**
13.61	**3.84**	**6.69**
14.31	**4.04**	**6.71**

Table B3- 7 Measured Data for Styrofoam

Material	**Width** ***(cm)***	**Length** ***(cm)***	**Thickness** ***(cm)***
Styrofoam	121.8	197.7	9.90702

Frequency (GHz)	**Loss (dB)**	**Dielectric Constant**
0.52	**0.04**	**1.11**
1.22	**0.04**	**1.11**
1.92	**0.03**	**1.11**
2.62	**0.03**	**1.11**
3.32	**0.03**	**1.11**
4.02	**0.02**	**1.12**
4.72	**0.02**	**1.12**
5.42	**0.02**	**1.12**
6.12	**0.01**	**1.11**
6.82	**0.01**	**1.11**
7.52	**0.01**	**1.11**
8.22	**0.00**	**1.11**
8.92	**0.00**	**1.11**
9.62	**0.00**	**1.11**
10.32	**0.00**	**1.11**
11.02	**0.00**	**1.11**
11.72	**0.00**	**1.11**
12.42	**0.00**	**1.10**
13.12	**0.00**	**1.10**
13.82	**0.00**	**1.10**

Table B3- 8 Measured Data for Bricks

Material	Width (Thickness) *(cm)*	Length *(cm)*	Height *(cm)*
Bricks (single)	8.71474	19.8	5.82676

Frequency (GHz)	Loss (dB)	Dielectric Constant
1.01	**2.06**	**3.73**
1.31	**2.38**	**3.70**
1.61	**2.70**	**3.71**
1.91	**3.02**	**3.74**
2.21	**3.34**	**3.78**
2.51	**3.66**	**3.82**
2.81	**3.98**	**3.86**
3.11	**4.30**	**3.90**
3.41	**4.62**	**3.94**
3.71	**4.95**	**3.98**
4.01	**5.27**	**4.02**
4.31	**5.59**	**4.07**
4.61	**5.91**	**4.11**
4.91	**6.23**	**4.16**
5.21	**6.55**	**4.20**
5.51	**6.87**	**4.25**
5.81	**7.19**	**4.29**
6.11	**7.51**	**4.34**
6.41	**7.84**	**4.39**
6.71	**8.16**	**4.43**
7.01	**8.48**	**4.48**

Table B3- 9 Measured Data for Concrete Block

Material	**Width (Thickness) *(cm)***	**Length *(cm)***	**Height *(cm)***
Concrete Block	19.45	39.7	19.5

Frequency (GHz)	**Loss (dB)**	**Dielectric Constant**
2.02	**13.62**	**2.12**
2.32	**13.62**	**2.15**
2.62	**13.62**	**2.18**
2.92	**13.62**	**2.20**
3.22	**13.62**	**2.23**
3.52	**13.62**	**2.25**
3.82	**13.62**	**2.27**
4.12	**13.62**	**2.28**
4.42	**13.62**	**2.29**
4.72	**13.62**	**2.30**
5.02	**13.62**	**2.30**
5.32	**13.62**	**2.30**
5.62	**13.62**	**2.29**
5.92	**13.62**	**2.28**
6.22	**13.62**	**2.26**
6.52	**13.62**	**2.23**
6.82	**13.62**	**2.19**

B4. Material Pictures and Miscellaneous

(a) bricks moving wall

(b) blocks moving wall

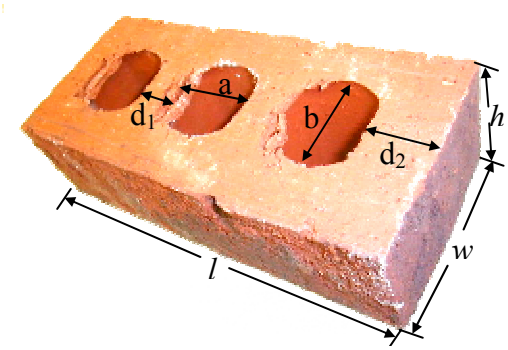

$w = 8.53542$ cm
$h = 5.82676$ cm
$b = 4.15036$ cm
$d_2 = 2.159$ cm

$l = 19.8$ cm
$a = 3.5179$ cm
$d_1 = 1.905$ cm

(c) single brick

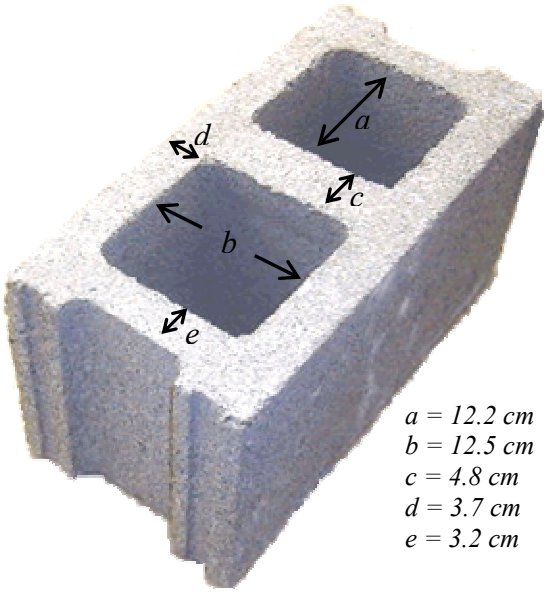

$a = 12.2$ cm
$b = 12.5$ cm
$c = 4.8$ cm
$d = 3.7$ cm
$e = 3.2$ cm

(d) single block

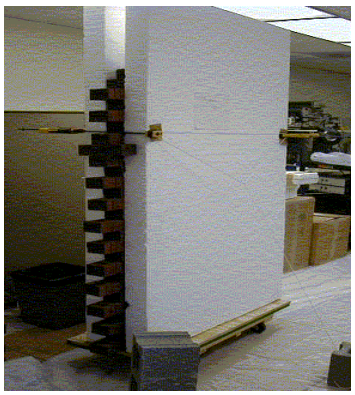

(e) moving bricks wall between two Styrofoam

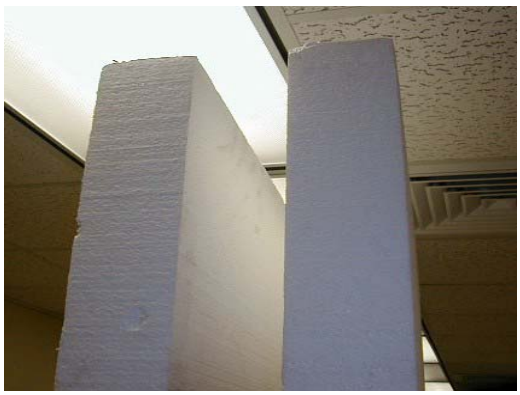

(f) Styrofoam (two slabs are shown)

Figure B3-1. Pictures for the bricks, blocks, Styrofoam and walls built out of them.

(a) wallboard (two are shown)

(b) door

(c) wood

(d) structure wood

(e) cloth office partition

(f) glass

(g) concrete pillar (TDL)

(h) reinforced concrete pillar (Whittemore)

Figure B3-2. Pictures for the wallboard, door, wood, structure wood, cloth office partitions, glass, and reinforced concrete pillars.

References

[Alq96] I. L. Al-Qadi, and S. M. Riad, "Characterization of Portland Cement Concrete: Electromagnetic & Ultrasonic Measurement Techniques", Virginia Polytechnic Institute and State University, submitted to National Science Foundation, September 1996.

[And02] C.R. Anderson, T. S. Rappaport, and et. al., "In-building wideband multipath characteristics at 2.5 & 60 GHz**",** Vehicular Technology Conference, 2002. Proceedings. VTC 2002-Fall. 2002 IEEE 56th , Volume: 1 , 2002. Page(s): 97-101.

[Aur96] F. J. Aurand, "Measurements of Transient Electromagnetic Propagation Through Concrete and Sand". Sandia National Laboratories, Sandia Report SAND96-2254 UC-706, Livermore, California 94550.

[Bak90] J. Baker-Jarvis, E. J. Vanzura, and W. A Kissck, "Improved Technique for Determining Complex Improved Technique for Determining Complex Permittivity with the Transmission/Reflection Method," *IEEE Transactions on Microwave Theory and Techniques*, vol. 38 , no. 8, August 1990.

[Bak98] J. Baker-Jarvis, *et al*, "Dielectric Characterization of Low-loss Materials A Comparison of Techniques," *IEEE Transactions on Dielectric and Electrical Insulation*, vol. 5, no. 4, August 1998.

[Cui00] I. Cuinas, and M. Sanchez, "Building Material Characterization from Complex Transmissivity Measurements at 5.8GHz," *IEEE Transaction on Antennas and Propagation*, vol. 48, no. 8, August 2000.

[Dan96] D.J. Daniels, *Surface-Penetrating Radar*, The institution of Electrical Engineers, London, United Kingdom, 1996.

[Dur98] G.Durgin, T.S. Rappaport, X, Hao, "Measurements and models for radio path loss and penetration loss in and around homes and trees at 5.85 GHz**",** Communications, IEEE Transactions on , Volume: 46 Issue: 11 , Nov. 1998. Page(s): 1484 –1496.

[Gey90] R. G. Geyer, "Dielectric Characterization and Reference Materials" National Institute of Standards and Technology (NIST): NIST Technical Note 1338, 1990.

[Gib99] T. Gibson and D. Jenn, "Prediction and Measurements of Wall Insertion Loss" *IEEE Transactions on Antennas and Propagation*, vol. 47, no. 1, Jan. 1999.

[Has93a] H. Hashemi "The Indoor Radio Propagation Channel" *Proceeding of the IEEE*, vol. 81, no. 7, pp 943-968, July 1993.

[Kra93] D. Kralj, and L. Carin, "Ultra-Wideband Characterization of Lossy Materials: Short-Pulse Microwave Measurements" Microwave Symposium Digest, IEEE MTT-S International, vol. 13, pp.1239 -1242 , 1993.

[Muq02a] A. Muqaibel, A Safaai-Jazi, and S. Riad, "Characterization of Dielectric Substrate Material Using Fork Resonator," 2002 IEEE AP-S International Symposium and USNC/*URSI NAtional Radio Science Meeting*, San Antonio, Texas.

[Muq02b] A. Muqaibel, A Safaai-Jazi, and S. Riad, "Fork Resonators for High Frequency Characterization of Dielectric Substrate Materials," submitted to the *IEEE Transaction on Instrumentation and Measurement.*

[Mat00] J. Matlacz, and K. D.Palmer, "Using offset Parabolic Reflector Antennas for Free Space Material Measurements," *IEEE Transaction on Instrumentation and Measurements*, vol. 49, no. 4, August 2000.

[Poz98] D. M. Pozar, *Microwave Engineering*, 2nd ed., John Wiley & sons, Inc., 1998.

[Sch93] R.A. Scholtz, "Multiple access with time-hopping impulse modulation," *Conference record Military: Communications Conference, Communications on the Move*, MILCOM '93, vol.2, 1993, pp. 447 –450

[Su96] W. Su, R. Mostafa, S.M. Riad, and I.L. Al-Qadi. 1996, " Characterization of Concrete Material Using TEM Horn Antennas." Presented at the URSI National Radio Science Meeting, Boulder, CO, January 11, 1996. Bradley Dept. of Electrical Engineering, Virginia Polytechnic Institute and State University, Blacksburg, VA.

[Yoh01] J.J. Yoho, *Physically-Based Realizable Modeling and Network Synthesis of Subscriber Loops Utilized in DSL Technology*, Ph.D Dissertation submitted to the ECE dep. at Virginia Tech., 2001

[Zha01] J. Zhang, M. Nakhash, and Y. Huang, "In-Situ Characterization of Building Materials," *11th International Conference on Antennas and Propagation*, Conference Publication no. 480, April 17-20, 2001.